International Journal of Multiphase Flow 37 (2011) 812–830

Contents lists available at ScienceDirect

International Journal of Multiphase Flow

journal homepage: www.elsevier.com/locate/ijmulflow

Interfacial instability in turbulent flow over a liquid film in a channel

L. Ó Náraigh [a,b,*], P.D.M. Spelt [a,c], O.K. Matar [a], T.A. Zaki [d]

[a] Department of Chemical Engineering, Imperial College London, London SW7 2AZ, United Kingdom
[b] School of Mathematical Sciences, University College Dublin, Belfield, Dublin 4, Ireland
[c] Université de Lyon 1 and Laboratoire de la Mécanique des Fluides & d'Acoustique, CNRS, Ecole Centrale Lyon, Ecully, France
[d] Department of Mechanical Engineering, Imperial College London, London SW7 2AZ, United Kingdom

ARTICLE INFO

Article history:
Received 7 May 2010
Received in revised form 24 February 2011
Accepted 27 February 2011
Available online 6 March 2011

Keywords:
Interfacial instability
Turbulence
Two-phase flow

ABSTRACT

We revisit the stability of a deformable interface that separates a fully-developed turbulent gas flow from a thin layer of laminar liquid. Although this problem has received considerable attention previously, a model that requires no fitting parameters and that uses a base-state profile that has been validated against experiments is, as yet, unavailable. Furthermore, the significance of wave-induced perturbations in turbulent stresses remains unclear. To address these outstanding issues, we investigate this problem and introduce a turbulent base-state velocity that requires specification of a flow rate or a pressure drop only; no adjustable parameters are necessary. This base state is validated extensively against available experimental data as well as the results of direct numerical simulations. In addition, the effect of perturbations in the turbulent stress distributions is investigated, and demonstrated to be small for cases wherein the liquid layer is thin. The detailed modelling of the liquid layer also elicits two unstable modes, 'interfacial' and 'internal', with the former being the more dominant of the two. We show that it is possible for interfacial roughness to reduce the growth rate of the interfacial mode in relation to that of the internal one, promoting the latter, to the status of most dangerous mode. Additionally, we introduce an approximate measure to distinguish between 'slow' and 'fast' waves, the latter being the case for 'critical-layer'-induced instabilities; we demonstrate that for the parameter ranges studied, the large majority of the waves are 'slow'. Finally, comparisons of our linear stability predictions are made with experimental data in terms of critical parameters for onset of wave-formation, wave speeds and wavelengths; these yield agreement within the bounds of experimental error.

1. Introduction

A linear stability analysis of small-amplitude waves on an otherwise flat liquid film would provide a powerful tool in understanding and modelling the onset of droplet entrainment from a liquid layer by a shearing superposed turbulent gas flow, which has numerous industrial applications (e.g. Hall-Taylor and Hewitt (1970)). Furthermore, this would serve as a benchmark for direct numerical simulations of two-layer flows, as in Boeck et al. (2007), Valluri et al. (2008), Fuster et al. (2009), Valluri et al. (2010) for laminar flows. Although various authors have worked on this problem (Miesen and Boersma, 1995; Kuru et al., 1995), several difficulties have arisen in these studies, preventing them from being of direct use as benchmark tests for direct numerical simulations of turbulent stratified channel flows and industrial applications. First, a robust model for a base-state velocity profile that has been tested against experiments and numerical simulations is not available, and its detailed modelling turns out to be important. Second, the base state should not require specification of any fitting parameters: merely the flow rate or imposed pressure drop (along with the physical and geometrical properties) should suffice. Previous models lack at least one of these aspects; the base-state model proposed here satisfies all of these criteria. A second motivation for this study is to ascertain the role of perturbations in turbulent stresses, which are caused by the presence of waves. These could potentially feed back to the growth rate and speed of the wave even in a linear analysis.

In previous work, a 'lin-log' base-state profile has been used in a boundary-layer setting, and either the friction velocity U_* or the friction factor C_f was guessed (Miesen and Boersma, 1995). Others have adopted an empirical profile, the validity of which is unclear (Kuru et al., 1995). Here, we derive a base-state model that contains no free parameters: the friction velocity is determined as a function of Reynolds number. We develop our base state starting from a rigorously validated model (that of Biberg (2007)), and generalise it in order to take account of the near-interfacial zone. This is an important step since this region is significant for instabilities driven by viscosity contrasts Yih (1967); as will be shown below,

* Corresponding author at: Department of Chemical Engineering, Imperial College London, London SW7 2AZ, United Kingdom.
E-mail address: lennon.onaraigh@ucd.ie (L. Ó Náraigh).

0301-9322/$ - see front matter © 2011 Elsevier Ltd. All rights reserved.
doi:10.1016/j.ijmultiphaseflow.2011.02.010

this is the dominant mode for our system over the range of parameters studied in the present work. We compare the resulting model with direct numerical simulations and experiments. Furthermore, our model contains no logarithmic singularities: full modelling of the viscous sublayers is provided, in contrast to the model of Biberg (2007).

To explain the second motivation for the present study, we summarise the averaging technique presumed herein. Consider a large ensemble of realisations of a three-dimensional pressure-driven turbulent channel flow. The velocity field contains perturbations due to turbulence, and due to the presence of small-amplitude waves. At any time, a Fourier decomposition can be taken of the interface height and, simultaneously, of the velocity and pressure fields. These Fourier-decomposed velocity and pressure fields can be averaged over the ensemble of realisations (as well as over the spanwise direction). These ensemble-averaged velocity and pressure fields are not uni-directional, but are distorted due to the presence of the corresponding (normal mode) interfacial wave. Example fields that have been obtained in conceptually the same manner from DNS (albeit for turbulent flow over a wavy wall) can be found in the paper of Sullivan et al. (2000). In the present study, results are presented (and compared) from several RANS models. A significant issue here is that such wave-induced perturbation stresses may, in principle, affect the growth rate and speed of waves. Questions concerning the importance of these stresses have been much debated in the literature (Miles, 1957; Belcher and Hunt, 1993; Belcher et al., 1994; Kuru et al., 1995; Janssen, 2004). Previous studies on sheared liquid films have not accounted for these effects, hence the significance of these stresses is not known at present. The present study does at last provide convincing evidence that these are indeed not important in the determination of wave speed and growth rate for sheared thin films. The linear stability analysis and assessment of the significance of perturbation turbulent stresses (perturbed turbulent stresses) are the subject of Section 3.

At least four mechanisms have been reported to generate instability in a laminar liquid layer sheared by an external turbulent gas flow. The first kind, called the *critical-layer instability*, was identified by Miles (1957). The transfer of energy from the mean flow into the wave perturbations is governed by the sign of the second derivative of the base-state flow at the critical layer – the height where the wave speed and the base-state velocity match. Another kind of instability, called the *viscosity-contrast mechanism*, was identified by Yih (1967), alluded to above: here, the instability arises due to the jump in the viscosity across the interface. In addition, instability can occur because of direct forcing by turbulent pressure oscillations in the gas (Phillips, 1957). The so-called *internal mode* (Miesen and Boersma, 1995; Boomkamp and Miesen, 1996) is observed when the bottom layer is laminar. This mode derives its energy both from the interface, and from conditions in the bulk of the bottom layer. Thus, this mode persists even when the upper layer is void (Miesen and Boersma, 1995) and has the characteristics of a Tollmien–Schlichting wave, depending sensitively on the viscosity contrast. Belcher and Hunt (1993) proposed that the turbulent stresses could produce the same effect, although in this paper, we find that the viscous stresses are dominant in the creation of the instability, at least under the thin-film parameter regime studied here. Finally, we note here that approximate mechanisms such as those identified in Kelvin–Helmholtz-type theories, although perhaps relevant in large-amplitude waves, do not arise in the full linearised problem wherein viscous effects are fully accounted for Boomkamp and Miesen (1996).

The paper is organised as follows. The base-state (flat interface) model is presented in Section 2. In Section 3, we carry out preliminary linear stability calculations to investigate the stability of the flat interface, and to assess the importance of the perturbed turbulent stresses. The implications of our stability analyses are discussed in Section 4: we investigate the source of the instability, the possibility of mode competition, and the importance of interfacial roughness. We validate the linear stability against experimental evidence, and find good agreement in Secion 5. Concluding remarks are in Section 6.

2. Base-state formulation

Given a flat-interface *base state* of a two-layer, pressure-driven channel flow (Fig. 1), the growth rate of small-amplitude waves on the interface depends sensitively on the details on the base state. We therefore focus on deriving an accurate description of the base state. The resulting velocity profile, including the interfacial shear stress, are determined by a prescribed external pressure drop, without the need to introduce any *ad hoc* parameters. Our starting-point is the model of Biberg (2007), although we develop this model further by accounting for the presence of near-wall and near-interface *viscous sublayers*. The resulting model compares very favourably with direct numerical simulations (DNS) and with experiments, as we outline below. We begin by considering the case of a flat interface, before considering a base state with interfacial roughness in Section 2.2.

2.1. Flat interface

Here, we consider a base state characterised by a steady, spatially-uniform, interface separating a turbulent layer overlying a thin, laminar one in a rectangular channel; both layers are assumed to be fully-developed. We use a Cartesian coordinate system, (x,z), to examine this two-dimensional flow, wherein the lower and upper layers occupy the regions $-d_L \leqslant z \leqslant 0$ and $0 \leqslant z \leqslant h$, respectively; the flat interface is located at $z = 0$ and the upper and lower walls at $z = h$ and $z = -d_L$, respectively. For ease of comparison with experiments, the focus of this paper is on laminar–turbulent systems; the generalisation to turbulent–turbulent layers is straightforward. Furthermore, the parameter ranges investigated below are characteristic of air–water systems, hence for the remainder of this paper, we will refer to the upper and lower layers as the 'gas' and 'liquid' layers, respectively.

In the base state, the flow is uni-directional in the horizontal, x-direction. In the gas layer, near the gas–liquid interface and the gas–wall boundary, the flow profile is linear, and the viscous scale exceeds the characteristic length scale of the turbulence (Monin and Yaglom, 1971; Pope, 2000); this is indicated in Fig. 1. In the bulk of the gas region, the flow possesses a logarithmic profile (Monin and Yaglom, 1971; Pope, 2000). We assume that the gas–liquid interface is smooth, although the model can account for interfacial roughness; this will be discussed in Section 2.2.

2.1.1. Liquid layer

In the liquid film, the Navier–Stokes equations reduce to the following standard balance law between pressure and viscous forces:

$$\mu_L \frac{\partial^2 U_0}{\partial z^2} - \frac{\partial P_0}{\partial x} = 0, \tag{1}$$

where $U_0(z)$, P_0, and μ_L denote the liquid mean flow velocity, pressure, and viscosity, respectively. We integrate Eq. (1) and apply the following boundary conditions, which correspond, respectively, to continuity of tangential stress at the interface, $z = 0$, and no-slip at the channel bottom wall, $z = -d_L$:

$$\mu_L \left.\frac{\partial U_0}{\partial z}\right|_{z=0} = \tau_i = \rho_G U_{*i}^2, \quad U_0(-d_L) = 0, \tag{2}$$

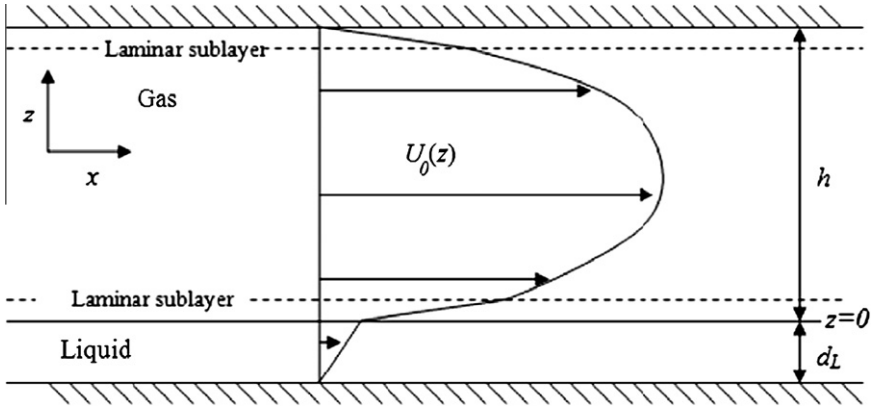

Fig. 1. A schematic representation of the base flow. The liquid layer is laminar, while the gas layer exhibits fully-developed turbulence, described here by a Reynolds-averaged velocity profile. A pressure gradient in the x-direction drives the flow.

where we have assumed that the pressure gradient does not depend on z. In Eq. (2), ρ_G denotes the gas density, τ_i is the interfacial stress and U_{*i} is the interfacial friction velocity on the gas side. An expression for U_{*i} in terms of $\partial P_0/\partial x$ will be obtained below. Application of the boundary conditions (2) yields the following relation for U_0:

$$U_0(z) = \frac{1}{2\mu_L}\frac{\partial P_0}{\partial x}\left(z^2 - d_L^2\right) + \frac{\tau_i}{\mu_L}(z + d_L). \tag{3}$$

We nondimensionalise on the scale U_p, where

$$U_p = \sqrt{\frac{h}{\rho_G}\left|\frac{\partial P_0}{\partial x}\right|}; \tag{4}$$

this scale is characteristic of a flow driven by a pressure gradient. The rescaling gives

$$\widetilde{U}_0 = \frac{1}{m}\left[-\frac{1}{2}Re(\tilde{z}^2 - \delta^2) + \frac{Re_*^2}{Re}(\tilde{z} + \delta)\right], \quad \delta = \frac{d_L}{h}, \tag{5}$$

in which the tildes denote dimensionless quantities: $\widetilde{U} = U/U_p$, $\tilde{z} = z/h$, and $m = \mu_L/\mu_G$ is a viscosity ratio. The Reynolds numbers

$$Re = \frac{\rho_G U_p h}{\mu_G}, \quad Re_* = \frac{\rho_G U_{*i} h}{\mu_G},$$

are based on U_p and U_{*i}, respectively, the latter being a characteristic, interfacial frictional velocity. Note also the following relation for the dimensionless, base-state interfacial streamwise speed, which we will use below in deriving the base-state profile in the upper layer:

$$\widetilde{U}_0(0) = \frac{1}{m}\left(\frac{1}{2}\delta^2 Re + \frac{Re_*^2}{Re}\delta\right). \tag{6}$$

2.1.2. Gas layer

In the gas layer, the RANS equations reduce to the following:

$$\mu_G\frac{\partial U_0}{\partial z} + \tau_0 = \tau_i + \frac{\partial P_0}{\partial x}z, \tag{7}$$

where $U_0(z)$ is the base-state velocity in the gas, μ_G is the gas viscosity, and $\tau_0 = -\rho_G\langle u'w'\rangle$ is the turbulent shear stress due to the averaged effect of the turbulent fluctuating velocities, u' and w'. In channel flows, it is appropriate to model this term using an eddy-viscosity model (Monin and Yaglom, 1971). In mixing-length theory, the eddy viscosity depends on the local rate of strain (Bradshaw, 1974), which means that the turbulent shear stress depends on the square of the rate of strain. Instead of this standard mixing-length theory, we introduce an interpolation function for the eddy viscosity, based on the work of Biberg (2007), which mimics the ordinary mixing-length theory near the interface and near the wall, and transitions smoothly from having a positive slope near the interface, to having a negative slope near the wall. Thus, the turbulent shear stress is linear in the rate of strain, and

$$\tau_0 = \mu_T\frac{\partial U_0}{\partial z}, \quad \mu_T = \kappa\rho_G h U_{*w} G(\tilde{z})\psi_i(\tilde{z})\psi_w(1-\tilde{z}), \tag{8}$$

where μ_T is the eddy viscosity, U_{*w} is the friction velocity at the upper wall $\tilde{z} = 1$, and where $G(\tilde{z})$, $\psi_i(\tilde{z})$, and $\psi_w(1-\tilde{z})$ are functions to be determined; κ is the von Kármán constant, taken as to 0.4. Here ψ_i and ψ_w are interface and wall functions respectively, which damp the effects of turbulence to zero rapidly near the interface and the wall, while G is an interpolation function designed to reproduce the 'law of the wall' near the interface and the upper wall. The precise choices for G and the wall functions, given below, are confirmed by the agreement between our predictions of the base state and experiments and numerical simulation, as will be discussed later in this paper.

To generate a closure for U_0, we substitute Eq. (8) into Eq. (7) and integrate with respect to z:

$$\begin{aligned} U_0(z) &= U_0(0) + \tau_i h\int_0^{z/h}\frac{\left(1 + \frac{h}{\tau_i}\frac{\partial P_0}{\partial x}s\right)ds}{\mu_G + \kappa\rho_G h U_{*w}G(s)\psi_i(s)\psi_w(1-s)}, \\ &= U_0(0) + \tau_i h\int_0^{z/h}\frac{\left(1 + \frac{h}{\tau_i}\frac{\partial P_0}{\partial x}s\right)ds}{\mu_G + \frac{\kappa\rho_G h U_{*i}}{\sqrt{|R|}}G(s)\psi_i(s)\psi_w(1-s)}, \end{aligned} \tag{9}$$

where $R = \tau_i/\tau_w$. We nondimensionalise Eq. (9) and make use of Eq. (6) to obtain

$$\widetilde{U}_0(\tilde{z}) = \frac{1}{m}\left(\frac{1}{2}Re\delta^2 + \frac{Re_*^2}{Re}\delta\right) + \frac{Re_*^2}{Re}\int_0^{\tilde{z}}\frac{\left(1 - \frac{Re^2}{Re_*^2}s\right)ds}{1 + \frac{\kappa Re_*}{\sqrt{|R|}}G(s)\psi_i(s)\psi_w(1-s)}. \tag{10}$$

The ratio R can be obtained in closed form as follows. Since

$$\begin{aligned} \tau(z) &= \tau_i + \frac{\partial P_0}{\partial x}z, \\ &= -\tau_w + \frac{\partial P_0}{\partial x}(z - h), \end{aligned}$$

these formulas can be equated to give

$$\tau_i = -\tau_w - \frac{\partial P_0}{\partial x}h,$$

or,

$$-\frac{\tau_w}{\tau_i} = 1 + \frac{\partial P_0}{\partial x}\frac{h}{\tau_i} = 1 - \left(\frac{Re}{Re_*}\right)^2,$$

hence,

$$|R| = \left|1 - \left(\frac{Re}{Re_*}\right)^2\right|^{-1}.$$

To determine Re_*, we make use of the no-slip condition at the upper channel wall, $\tilde{z} = 1$, $\widetilde{U}_0(1; Re_*) = 0$:

$$\frac{1}{m}\left(\frac{1}{2}\delta^2 Re + \frac{Re_*^2}{Re}\delta\right) + \left\{\frac{Re_*^2}{Re}\int_0^1 \frac{\left(1 - \frac{Re_*^2}{Re_*^2}s\right)\mathrm{d}s}{1 + \frac{\kappa Re_*}{\sqrt{|R|}}G(s)\psi_{\mathrm{i}}(s)\psi_{\mathrm{w}}(1-s)}\right\}_{|R| = \left|1-\left(\frac{Re}{Re_*}\right)^2\right|^{-1}} = 0. \quad (11)$$

Solution of this equation yields a relationship between Re_* and Re, δ, and m.

We now select G as follows:

$$G(s) = s(1-s)\underbrace{\left[\frac{s^3 + |R|^{5/2}(1-s)^3}{R^2(1-s)^2 + Rs(1-s) + s^2}\right]}_{=\mathscr{F}(s)}], \quad 0 \leqslant s \leqslant 1. \quad (12)$$

We show below that this function reproduces a logarithmic velocity profile near the gas–liquid interface and upper channel wall. For the wall functions, ψ_{i} and ψ_{w}, we use standard van Driest-type relations (Pope, 2000):

$$\psi_{\mathrm{i}}(s) = 1 - e^{-s^n/A_{\mathrm{i}}}, \quad \psi_{\mathrm{w}}(1-s) = 1 - e^{-(1-s)^n/A_{\mathrm{w}}}, \quad (13)$$

where n, A_{i}, and A_{w} are input parameters. These parameters will be fixed below and will *not* be adjusted in order to maximise agreement between modelling predictions and experimental data.

2.1.3. Limiting behaviour

Based on the derivation detailed above, we have the following velocity profile in the base state:

$$\widetilde{U}_0(\tilde{z}) = \begin{cases} \frac{1}{m}\left[-\frac{1}{2}Re(\tilde{z}^2 - \delta^2) + \frac{Re_*^2}{Re}(\tilde{z} + \delta)\right], & -\delta \leqslant \tilde{z} \leqslant 0, \\ \frac{1}{m}\left(\frac{1}{2}\delta^2 Re + \frac{Re_*^2}{Re}\delta\right) + \frac{Re_*^2}{Re}\int_0^{\tilde{z}} \frac{\left(1 - \frac{Re_*^2}{Re_*^2}s\right)\mathrm{d}s}{1 + \frac{\kappa Re_*}{\sqrt{|R|}}G(s)\psi_{\mathrm{i}}(s)\psi_{\mathrm{w}}(1-s)}, & 0 \leqslant \tilde{z} \leqslant 1. \end{cases} \quad (14)$$

To examine the limiting behaviour of the gas velocity profile in the viscous sublayers near the gas–liquid interface, $\tilde{z} = 0$, and upper channel wall, $\tilde{z} = 1$, we first note that the functions ψ_{i} and ψ_{w} transition rapidly from $\psi_{\mathrm{i}}(0) = 0$ and $\psi_{\mathrm{w}}(1) = 0$ to unity, across a width given by

$$\frac{d_{\mathrm{v}}}{h} = \frac{v_G}{hU_{*\mathrm{i}}} = \frac{1}{Re_*}, \quad \text{and} \quad \frac{d_{\mathrm{v,w}}}{h} = \frac{v_G}{hU_{*\mathrm{w}}} = \frac{|R|}{Re_*}, \quad (15)$$

respectively; here, the value of $A_{\mathrm{i}}(A_{\mathrm{w}})$ is related to the width of $\psi_{\mathrm{i}}(\psi_{\mathrm{w}})$. Thus to determine the behaviour of U_0 near the gas–liquid interface, that is, for $0 \sim \tilde{z} \ll 1/Re_*$, we make use of the fact that, in this region, $\psi_{\mathrm{i}} \sim 0$, $\psi_{\mathrm{w}} \sim 1 - \exp(-1/A_{\mathrm{w}})$, and $G \sim 0$, hence

$$\widetilde{U}_0 \sim \frac{1}{m}\left(\frac{1}{2}\delta^2 Re + \frac{Re_*^2}{Re}\delta\right) + \frac{Re_*^2}{Re}\int_0^{\tilde{z}} \mathrm{d}s = \frac{1}{m}\left(\frac{1}{2}\delta^2 Re + \frac{Re_*^2}{Re}\delta\right) + \frac{Re_*^2}{Re}\tilde{z}. \quad (16)$$

Similar arguments demonstrate the existence of another linear layer near the upper channel wall, which is the appropriate behaviour one expects in viscous sublayers adjacent to boundaries.

Next, we determine the behaviour of $\widetilde{U}_0$ in regions that lie outside the viscous sublayers, located near $\tilde{z} = 0$ and $\tilde{z} = 1$, but still far from $\tilde{z} = h_m/h$,

$$h_m = h\frac{Re_*^2}{Re^2}, \quad (17)$$

where h_m/h denotes the midpoint of the region $0 \leqslant \tilde{z} \leqslant 1$ at which

$$\frac{\partial \widetilde{U}_0}{\partial \tilde{z}} \propto 1 - \frac{Re^2}{Re_*^2}\tilde{z} = 0. \quad (18)$$

Thus, for regions sandwiched between the viscous sublayer near the gas–liquid interface and $\tilde{z} = h_m/h$, that is, for

$$\frac{1}{Re_*} \ll \tilde{z} \ll \frac{Re_*^2}{Re^2},$$

we have $G \sim |R|^{1/2}z$, $(\psi_{\mathrm{i}}, \psi_{\mathrm{w}}) \sim 1$. Substitution of these results into Eq. (14) yields

$$\widetilde{U}_0 \sim \frac{1}{m}\left(\frac{1}{2}\delta^2 Re + \frac{Re_{ast}^2}{Re}\delta\right) + \frac{Re_*^2}{Re}\int^{\tilde{z}} \frac{\mathrm{d}s}{\kappa Re_* s} = \frac{1}{m}\left(\frac{1}{2}\delta^2 Re + \frac{Re_*^2}{Re}\delta\right) + \frac{Re_*}{\kappa Re}\ln(\tilde{z}). \quad (19)$$

A similar calculation near $\tilde{z} = 1$ establishes the existence of a log layer close to the upper channel wall, which, once again, is the appropriate behaviour one expects in the transition region between viscous sublayers and the channel core. The expression for G, Eq. (12), was first derived by Biberg (2007) and is generalised here by accounting for the dynamically important viscous sublayers neglected in that work. This is essential in order to avoid the logarithmic singularities that would have otherwise arisen near $\tilde{z} = (0, 1)$.

2.1.4. Determination of the model constants

We establish the values of $A_{\mathrm{i,w}}$ and n in Eq. (13). By combining Eqs. (8) and (13) in a Taylor expansion near $\tilde{z} = 0$, we obtain the following form for the Reynolds stress:

$$\frac{\tau_0}{\rho_G U_p^2} \sim \kappa\frac{Re_*^3}{Re^2}\frac{\tilde{z}^{n+1}}{A_{\mathrm{i}}}.$$

A good approximation to the interface in two-phase turbulence with a large density contrast is, in fact, a solid wall (Fulgosi et al., 2002). Thus, we set $n = 2$, the value appropriate for wall-bounded turbulence (Pope, 2000). In a similar manner, we fix A_{i} and A_{w} with reference to single-phase theory, wherein there is a one-to-one correspondence between the values of A_{i} and A_{w} and the additive constant B in the single-phase log-law. With $\kappa = 0.4$, the specification

$$A_{\mathrm{i,w}} = e^{6.3}Re_{*\mathrm{i,w}}^{-2} \quad (20)$$

corresponds to the known value $B = 5.3$. It is this relationship that we use throughout our study. Thus, the values of n and $A_{i,w}$ have been fixed and will not be adjusted in the rest of the paper, particularly when comparing our predictions with experimental observations.

We plot in Fig. 2 the base-state velocity profile, $\widetilde{U}_0$, for $Re = 1000$, for which the corresponding superficial Reynolds number based on the gas flow rate is approximately 12,000. The near-interfacial viscous and logarithmic layers are visible in Fig. 2b. Using Eq. (11), we can determine the friction Reynolds number, Re_*, as a function Re, which we treat as a 'control parameter'; this relation is shown in Fig. 3a. We can also determine the dependence of a 'liquid Reynolds number', defined as

$$Re_L = \frac{\rho_L d_L U_{\mathrm{i}}}{\mu_L}, \quad U_{\mathrm{i}} = \frac{\tau_{\mathrm{i}} d_L}{\mu_L} \quad (21)$$

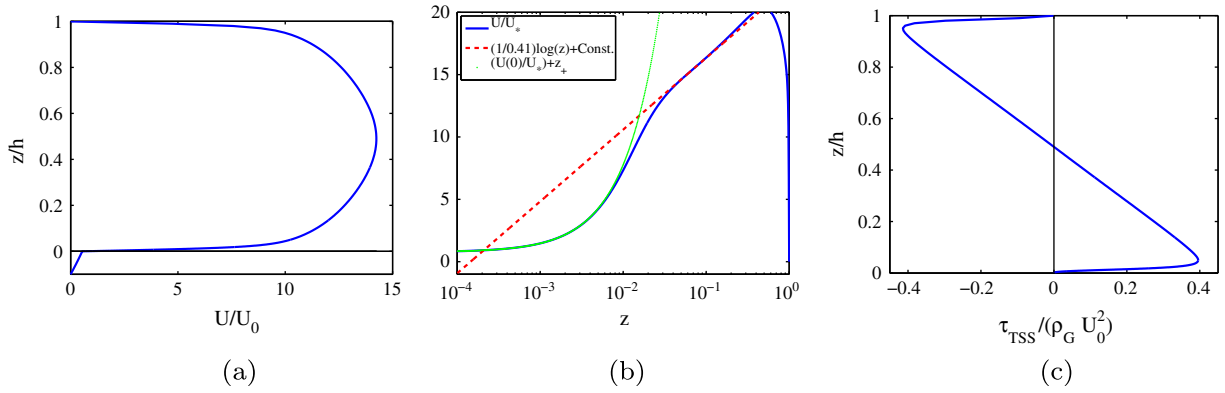

Fig. 2. Base-state profiles for the parameter values $(\mu_L/\mu_G, \rho_L/\rho_G, d_L/h)$: = (m, r, δ) = (100, 1000, 0.1), and Re = 1000. (a) The mean velocity profile; (b) the mean velocity profile in wall units, showing the logarithmic and viscous layers (the viscous layer has a wall-unit thickness of approximately 5); (c) the Reynolds-stress profile corresponding to the basic velocity.

on Re; this is shown in Fig. 3b. The relationship shown in Fig. 3a is approximately linear, a consequence of the very small velocities in the liquid, compared with the maximal gas velocity. Thus, the gas layer closely resembles single-phase channel flow, and the condition $U_0(0) \ll U_{\max}$ mimics the zero interfacial-velocity condition in the single-phase channel. The channel midpoint where $\partial U_0/\partial z = 0$ is thus approximately equal to half the gas-layer depth $h_m \approx h/2$. Using this guess in Eq. (17) gives $Re_* \approx Re/\sqrt{2}$, which is close to the slope calculated in the figure. Having now fully characterised the smooth, flat-interface base state (Figs. 2 and 3), we discuss a way to model the scenario wherein the interface possesses a small amount of roughness generated by the turbulence.

2.2. Interfacial roughness

In the preceding exposition, we have been concerned with flow profiles where the interface is perfectly smooth. Now, we allow for interfacial roughness by modifying the eddy-viscosity law (8) and (12). The work of Lin et al. (2008) gives one possible explanation for the generation of such roughness. This indicates that the so-called Phillips mechanism (Phillips, 1957) may be important, whereby instantaneous turbulent pressure fluctuations lead to a regime of linear wave growth. This is later followed by an exponential growth regime, which is primarily governed by the disturbances in the flow induced by the waves themselves. In the present context, we regard the interfacial roughness as a consequence of the gas-phase turbulence, which then acts on the interfacial waves, thereby modifying the growth in the wave amplitude.

To model interfacial roughness, we use an eddy-viscosity model like that of Biberg (2007). Such a model has the effect of shrinking the viscous sublayer near the interface. In our formalism, this is achieved by altering the form of the mixing length near the interface: before it was

$$\mathscr{L} \sim z\psi_i(z/h), \quad \text{as } z \to 0,$$

where $\psi_i(z/h)$ is the damping function that operates in the near-wall region $z \lesssim 5U_{*i}/\nu_G$; now, instead, we propose the behaviour

$$\mathscr{L} \sim \ell_i, \quad \text{as } z \to 0.$$

Thus,

$$\frac{\tau_0}{\rho_G U_p^2} = \frac{\kappa}{\sqrt{|R|}}[\tilde{z} + K(1-\tilde{z})](1-\tilde{z})\psi_w(1-\tilde{z})\mathscr{V}(\tilde{z})\frac{d\tilde{U}_0}{d\tilde{z}}, \quad \tilde{z} = z/h,$$
$$= \frac{\kappa}{\sqrt{|R|}}G(\tilde{z}; K)\psi_w(1-\tilde{z})\frac{d\tilde{U}_0}{d\tilde{z}}, \tag{22}$$

where $K = \ell_i/(\kappa h)$ is the nondimensional interfacial roughness parameter. In all but one subsection of the paper, we focus on the case wherein the base-state interface is smooth; only in Section 4.4 do we investigate the effects of interfacial roughness on the linear stability of the two-phase interface.

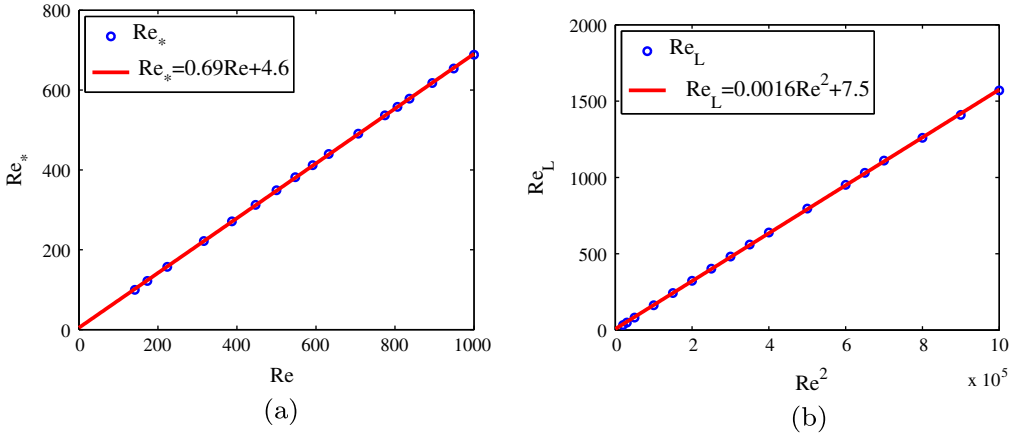

Fig. 3. The dependence of Re_* and Re_L on Re (circles) shown in (a) and (b), respectively, with δ = 0.1 and (m, r) = (55, 1000). Also shown in both panels are lines of best fit (lines).

2.3. Slow and fast waves

Our model gives a way of predicting the values of (Re, d_L) for which the critical-layer instability could be relevant. This mechanism depends sensitively on the shape of the base state in the gas layer, and causes a tiny wave-like perturbation at the interface to grow in time when $(\mathrm{d}^2U_0/\mathrm{d}z^2)_{z=z_c} < 0$, where the critical height z_c is the root of the equation $U_G(z) = c$, and where c is the wave-propagation speed (tildes over nondimensional quantities are omitted).

First, we describe the wave speeds for which the critical-layer mechanism plays no role. Our discussion is based on the fact that if the critical layer lies inside the viscous sublayer, which is five interfacial units in extent, then the curvature of the mean profile therein is negligible, and the critical-layer mechanism is unimportant. Thus, in order for the critical-layer mechanism to play no role,

$$z_c^+ = Re_* z_c \leqslant 5.$$

In this limiting case, the velocity profile in the vicinity of the critical layer is linear:

$$U(z_c) \approx U_0(0) + \frac{Re_*^2}{Re} z_c = U_0(0) + \frac{Re_*}{Re} z_c^+, \tag{23a}$$

We solve the critical-layer equation $U_0(z_c) = c$ in the limiting regime (23a). The result is

$$z_c^+ = \frac{Re}{Re_*}(c - U_0(0)),$$

which is true provided the right-hand-side never exceeds five wall units. Thus, there is an exact criterion for the waves to be slow: $z_c^+ \leqslant 5$, or

$$c - U_0(0) \leqslant \frac{5Re}{Re_*}. \tag{23b}$$

Eq. (23b) gives a formal definition of a 'slow' wave. We use the thin-film approximation $Re_* \approx Re/\sqrt{2}$ and redimensionalise the slow-wave criterion; this condition then reduces to

$$\frac{c - U_0(0)}{U_p} \lesssim \frac{5}{\sqrt{2}} = O(1). \tag{23c}$$

Next, we estimate the wave speed c, which we denote by c_{est}, using the formula for gravity-capillary waves on a quiescent free surface (recall that the tilde is used to denote dimensionless variables) (Acheson, 1990):

$$\frac{c_{\mathrm{est}}}{U_p} = \frac{1}{Re}\sqrt{\frac{gh}{(\mu_G/\rho_G h)^2}\frac{r-1}{r+1}\frac{1}{\tilde{\alpha}} + \frac{1}{r+1}\frac{\sigma}{\mu_G^2/\rho_G h}\tilde{\alpha}}\sqrt{\tanh(\tilde{\alpha}\delta)}. \tag{24}$$

This formula holds exactly only for inviscid fluids with an infinite upper layer (the prefactor $1/Re$ is due to the choice of nondimensionalisation). However, we have tested the accuracy of the formula in a number of cases (see Section 4.1), where it gives an order-of-magnitude prediction of the wave speed. The true value of the wave speed and the estimate agree at short wavelengths, which is precisely the limit where interfacial waves show inviscid behaviour. Finally, we substitute the values from Table 1 into Eq. 24 and obtain a graphical description of the boundary between slow and fast waves, as a function of the parameters $(d_L, \delta, Re, \alpha)$ (Fig. 4). When $c_{\mathrm{est}}/U_p \ll 1$, we expect the critical-layer mechanism to be unimportant. This is precisely the regime of small d_L-values and high Reynolds numbers, which is the subject of this report. According to the classification of Boomkamp and Miesen (1996), the other two mechanisms of instability that exist for two-phase flow are the viscosity-contrast instability, and the liquid internal mode. We must therefore be on the lookout for these instabilities in any linear stability based on the velocity profile derived herein.

Table 1
Table of parameter values used to estimate the wave speed.

Symbol	Numerical value, S.I. Units
μ_G	1.8×10^{-5} Pa s
$m = \mu_L/\mu_G$	55
ρ_G	1 Kg m^{-3}
$r = \rho_L/\rho_G$	10^3
d_L	10^{-3}–10^{-2} m
$\delta = d_L/h$	0.1
g	9.8 ms^{-2}
σ	0.074 Nm^{-1}

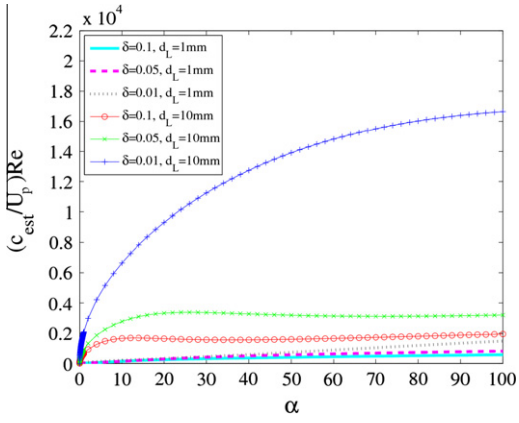

Fig. 4. The plot $(c_{\mathrm{est}}/U_p)Re = (c_{\mathrm{est}}/U_{*\ i})Re_*$ provides an estimate of the boundary between slow and fast waves.For very thin films ($d_L = 1$ mm), slow waves are guaranteed at almost all Reynolds numbers, while for thicker films ($d_L = 10$ mm) the waves are faster for all but the highest Reynolds numbers.

2.4. Comparison with experiments and DNS

To validate our model for the base state, we compare it with other studies of both single- and two-phase flow. A further comparison with studies of single-phase flow over a wavy wall (Zilker et al., 1976; Abrams and Hanratty, 1985 is provided in Appendix A. We first of all characterise the single-phase version of our model. This is obtained by setting $U_0(0) = 0$ and by ignoring the liquid layer. We compare with the experimental work of Willmarth et al. (1987), for single-phase pressure-driven channel flow. In the experiment, the input parameter is the Reynolds number based on the friction velocity, $Re_* = 1.143 \times 10^3$. In the single-phase version of our model, Eq. (17) reduces to $Re \approx \sqrt{2}Re_*$. Thus, the input parameter for the model is $Re = \sqrt{2} \times 1.143 \times 10^3$. From this model input, we derive a Reynolds number based on the mean velocity in the model:

$$Re_{\mathrm{m}} = \frac{\rho_G}{\mu_G}\int_0^h U_0(z)\ \mathrm{d}z.$$

The mean Reynolds number in the experiment was $Re_{\mathrm{m}} = 2.158 \times 10^4$; we compute Re_{m} to be 2.13×10^4, close to the experimental value. A plot of the profile is shown in Fig. 5: the model and the experimental data are in excellent agreement.

To validate the two-phase version of our model, we compare it with the work of Akai et al. (1980, 1981) who studied two-phase turbulence for an air-mercury system, where $m = 77$ and $r = 1.120 \times 10^4$ at room temperature. The liquid Reynolds number, based on the liquid-layer depth and the mean liquid velocity is set to $Re_{\mathrm{m},L} = 8040$ throughout the experiments. Because the liquid is no longer laminar, we apply the turbulence model Eq. (8) to both layers; the result is the following equation pair:

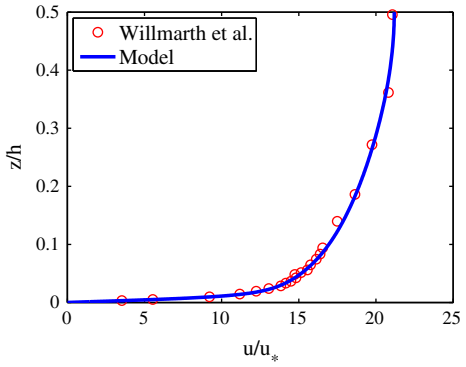

Fig. 5. A comparison with the work of Willmarth et al. (1987) for single-phase channel flow for $Re_m = 2130 \times 10^4$.

$$\widetilde{U}_0(\tilde{z}) = \begin{cases} \frac{Re_*^2}{Re_0} \int_{-\delta}^{\tilde{z}} \frac{\left(1-\frac{Re_0^2}{Re_*^2}s\right)\mathrm{d}s}{m+\frac{\kappa Re_* \delta r}{\sqrt{r|R_B|}} G_B(-s/\delta)\psi_B(s)}, \\ \quad -\delta \leqslant \tilde{z} \leqslant 0, \\ \frac{Re_*^2}{Re_0} \int_{-\delta}^{0} \frac{\left(1-\frac{Re_0^2}{Re_*^2}s\right)\mathrm{d}s}{m+\frac{\kappa Re_* \delta r}{\sqrt{r|R_B|}} G_B(-s/\delta)\psi_B(s)} + \frac{Re_*^2}{Re_0} \int_0^{\tilde{z}} \frac{\left(1-\frac{Re_0^2}{Re_*^2}s\right)\mathrm{d}s}{1+\frac{\kappa Re_*}{\sqrt{|R|}} G(s)\psi(s)\psi(1-s)}, \\ \quad 0 \leqslant \tilde{z} \leqslant 1, \end{cases} \tag{25}$$

where

$$R_B = -\frac{\tau_i}{\tau_{w,B}} = -\frac{1}{1+\frac{Re_0^2}{Re_*^2}\delta},$$

$$G_B(s) = s(1-s)\left[\frac{s^3 + |R_B|^{5/2}(1-s)^3}{R_B^2(1-s)^2 + R_B s(1-s) + s^2}\right], \quad 0 \leqslant s \leqslant 1,$$

$$\psi_B(s) = 1 - e^{-(s+\delta)^n / A_{vd,B}},$$

and where Re_* is determined as the root of the equation $\widetilde{U}(1; Re_*) = 0$. In the experiment, the input parameters are the gas-layer Reynolds number based on the mean gas velocity, and the liquid-layer Reynolds number:

$$Re_{m,G} = \frac{\rho_G}{\mu_G}\int_0^h U_0(z)\ \mathrm{d}z, \quad Re_{m,L} = \frac{\rho_L}{\mu_L}\int_{-d_L}^0 U_0(z)\ \mathrm{d}z.$$

For all the experiments, the liquid-layer Reynolds number is kept constant: $Re_{m,L} = 8040$, while $Re_{m,G}$ varies; we study the cases where $Re_{m,G} = 2340$ and 3690. The input parameters for the model are δ and Re. We obtain the δ-value that corresponds to $Re_{m,L}$ by an automated iteration procedure, wherein a trial value of Re_* is used to compute a trial value of δ, which in turn is used to compute a new value of Re_*. The iteration terminates when the refined value of δ corresponds to $Re_{m,L} = 8040$. Finally, the input parameter Re is obtained by trial-and-error, such that the value of Re corresponds to the correct value of $Re_{m,G}$. The implementation of this second step leaves the liquid-layer Reynolds number unchanged at $Re_{m,L} = 8040$. The results of this comparison are shown in Fig. 6, where excellent agreement is obtained, particularly in the gas phase. The agreement between the model and the experiments is as good as in the paper of Biberg (2007). This is not surprising, since our model is designed to replicate his in the log-law regions of the flow, and in the core regions. Indeed, we conclude from the near-exact agreement between our predictions and those of Biberg that our model inherits all the results he obtained from experimental comparisons. The added advantage of our model is that it can be continued down to the wall and interfacial zones.

Finally, to validate the near-interface region of the model, we compare it with the DNS results of Solbakken and Andersson (2004) for two-phase lubricated channel flow. To compare with their results, we take $\delta = 1/34$, $m = 2$, $r = 1$ (hence $\rho_L = \rho_G = \rho$), and

$$Re_\tau = \frac{\rho(h+2d_L)U_\tau}{2\mu_G} = \frac{\rho(h+2d_L)}{2\mu_G}\sqrt{\frac{h+2d_L}{2\rho}\left|\frac{\partial P_0}{\partial x}\right|} = 180.$$

To connect the model input parameter Re to the simulation input parameter Re_τ, we use the formulas

$$\frac{U_p}{U_\tau} = \sqrt{\frac{2}{2\delta+1}}, \quad \frac{Re}{Re_\tau} = \left(\frac{2}{2\delta+1}\right)^{3/2}.$$

Furthermore, we take

$$z^+ = \frac{z}{h}\frac{2Re_\tau}{2\delta+1}, \quad U^+ = \frac{U}{U_p}\sqrt{\frac{2}{2\delta+1}}.$$

The results of the comparison are shown in Fig. 7. There is excellent agreement, in particular near the interface. Further, comparisons for air–water flow (Adjoua and Magnaudet, 2009), and flow past wavy walls (Zilker et al., 1976; Abrams and Hanratty, 1985) are given in Appendix A.

In conclusion, we have formulated a model of two-phase interfacial flow where the upper layer is fully-developed and turbulent. The model requires no fitting parameters that are introduced. In particular, the model provides a correlation between the pressure drop and the interfacial shear stress. The agreement between our

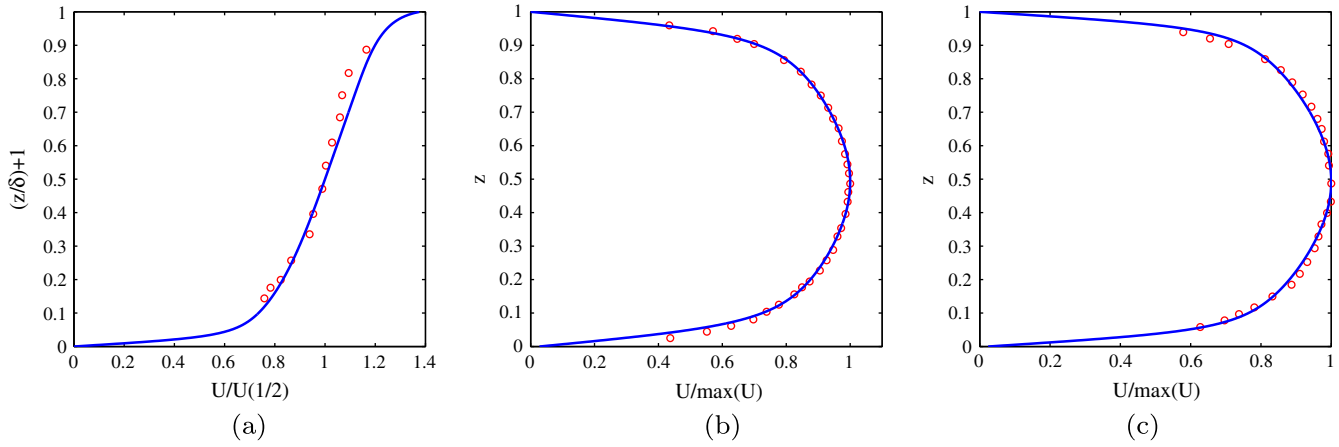

Fig. 6. A comparison with the work of Akai et al. (1980, 1981). Subfigures (a) and (b) show the comparison for $Re_{m,G} = 2340$; (c) shows the result for $Re_{m,G} = 3690$. Here $U(1/2)$ denotes the liquid-phase velocity half-way between the bottom wall and the interface. In both cases, $Re_{m,L} = 8040$.

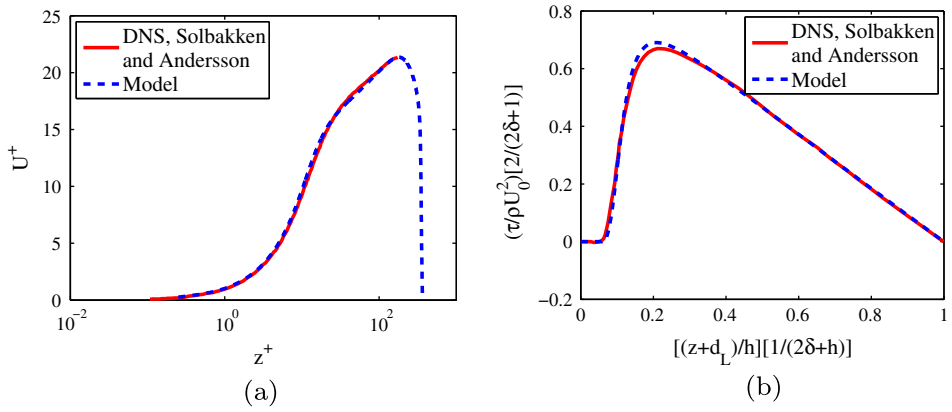

Fig. 7. Comparison with the results of Solbakken and Andersson (2004). (a) Broken-line: model velocity profile; solid line: DNS. (b) Reynolds-stress profile (the scaling of the axes corresponds to that used in the DNS paper).

model and experiments and DNS is convincing and inspires confidence in its use as a base state for the linear stability analysis which we now perform.

3. Linear stability analysis

In this section, we carry out a linear stability analysis based on the flat-interface base state derived above. We discuss in detail the modelling of the Reynolds stresses in the perturbation equations, the choice of physical parameters appropriate for modelling thin films in two-phase channel flow, and assess the importance of the Reynolds stresses in this scenario. Throughout this section, we work with a smooth-interface base state; only in Section 4.4 do we consider base states with interfacial roughness. We base the dynamical equations for the interfacial motion on the Reynolds-averaged Navier–Stokes (RANS) equations. We start by listing the relevant equations without assigning distinguishing decoration to designate the different phases; appropriate subscript notation is then introduced for the gas and liquid phases as appropriate.

3.1. Governing equations

The turbulent velocity is decomposed into an averaged component (U,W), and fluctuations. The averaged components depend on space and time through the RANS equations:

$$\rho\left(\frac{\partial U_i}{\partial t}+\boldsymbol{U}\cdot\nabla U_i\right)=-\frac{\partial P}{\partial x_i}+\frac{\partial T_{ij}^{(\mathrm{v})}}{\partial x_j}+\frac{\partial T_{ij}^{(\mathrm{t})}}{\partial x_j},\quad \text{sum over } j, \tag{26a}$$

$$\nabla\cdot\boldsymbol{U}=0, \tag{26b}$$

where

$$\boldsymbol{T}^{(\mathrm{v})}=\begin{pmatrix}2\mu U_x & \mu(U_z+W_x)\\ \mu(U_z+W_x) & 2\mu W_z\end{pmatrix},\quad \boldsymbol{T}^{(\mathrm{t})}=\begin{pmatrix}\sigma_1 & \tau\\ \tau & \sigma_2\end{pmatrix} \tag{26c}$$

represent the viscous and turbulent stress tensors in which τ denotes the turbulent shear stress, and σ_1 and σ_2 the turbulent normal stresses; here, the symbol σ should not be confused with that used to denote surface tension in the previous section. We have already used these equations to model the flat-interface base state of the two-phase system shown in Fig. 1. To understand the waves that develop on such an interface, we introduce a small disturbance that shifts the flat interface at $z=0$ to $z=\eta$ (the dimensionless wave elevation), where $|\eta|\ll 1$:

$$(U,W,P)=(U_0(z)+\delta u(x,z,t),\delta w(x,z,t),P_0(x)+\delta p(x,z,t)),$$
$$(\sigma_1,\sigma_2,\tau)=(\sigma_{01}+\delta\sigma_1,\sigma_{02}+\delta\sigma_2,\tau_0+\delta\tau),$$

where we denote base-state quantities by a subscript zero and the δ quantities are infinitesimally small disturbances; here, δ is not to be confused with the dimensionless film thickness. Since the flow is turbulent, and since the perturbations take the form of a wave with speed c, they must satisfy the RANS equations for a wave, $\partial/\partial t=-c\partial/\partial x$:

$$\rho\left[(U_0-c)\frac{\partial}{\partial x}\delta u+\frac{\mathrm{d}U_0}{\mathrm{d}z}\delta w\right]=-\frac{\partial}{\partial x}(\delta p-\delta\sigma_z)+\mu\left(\frac{\partial^2}{\partial x^2}+\frac{\partial^2}{\partial z^2}\right)\delta u+\frac{\partial}{\partial x}\delta\sigma+\frac{\partial}{\partial z}\delta\tau,$$

$$\rho(U_0-c)\frac{\partial}{\partial x}\delta w=-\frac{\partial}{\partial z}(\delta p-\delta\sigma_z)+\mu\left(\frac{\partial^2}{\partial x^2}+\frac{\partial^2}{\partial z^2}\right)\delta w+\frac{\partial}{\partial x}\delta\tau,$$

$$\frac{\partial}{\partial x}\delta u+\frac{\partial}{\partial z}\delta w=0.$$

where $\delta\sigma=\delta\sigma_1-\delta\sigma_2$. Using the streamfunction representation $(\delta u,\delta w)=(\partial\phi/\partial z,-\partial\phi/\partial x)$, and the normal-mode decomposition $(\phi,p,\sigma,\tau)(x,z,t)\propto e^{i\alpha(x-ct)}$ the perturbed RANS equations reduce to a single equation following the elimination of the pressure. In non-dimensional form, the equation governing the streamfunction in the gas phase is given by

$$i\alpha\left[(U_0-c)(D^2-\alpha^2)\phi_G-\frac{\mathrm{d}^2U_0}{\mathrm{d}z^2}\phi_G\right]=\frac{1}{Re}(D^2-\alpha^2)^2\phi_G+i\alpha D\delta\sigma+(D^2+\alpha^2)\delta\tau, \tag{27a}$$

where $D=\mathrm{d}/\mathrm{d}z$, and, as in the previous section, subscript 'G' designates gas-phase quantities. The analogous equation for the liquid reads

$$i\alpha r\left[(U_0-c)(D^2-\alpha^2)\phi_L-\frac{\mathrm{d}^2U_0}{\mathrm{d}z^2}\phi_L\right]=\frac{m}{Re}(D^2-\alpha^2)^2\phi_L. \tag{27b}$$

Eqs. (27) represent an Orr–Sommerfeld type of system (M'F Orr, 1907a,b; Orszag, 1971; Yiantsios and Higgins, 1988), with turbulent stresses in the gas that are additional to those that arise from viscous contributions. The problem of modelling these stresses in Eq. (27a) has received considerable attention in the literature (Belcher and Hunt, 1993, 1998; Belcher et al., 1994; Townsend, 1972; Ierley and Miles, 2001). In this section, we use two 'stationary' turbulent models from this literature to describe these stresses in which the eddy turnover frequency $U_{*i}/(\kappa z)$ exceeds the advection frequency

$\alpha|U_G(z) - c|$ (Belcher and Hunt, 1993; Belcher et al., 1994; Janssen, 2004) in the gas phase. The use of such models is appropriate for 'slow' waves because the dynamically important region for the instability is located very close to the interface, on the gas side. These 'stationary' models are discussed next.

3.2. The visco-elastic model

This turbulence model is a 'stationary' one whose starting-point is the following standard description for the perturbation-induced turbulent kinetic energy (TKE) (Pope, 2000):

$$\underbrace{\left(\frac{\partial}{\partial t}+U_0\frac{\partial}{\partial x}\right)\delta k+\delta w\frac{\mathrm{d}k_0}{\mathrm{d}z}}_{\text{Advection}}=\underbrace{\left(\mu_T+\frac{1}{Re}\right)\nabla^2\delta k+\frac{\mathrm{d}\mu_T}{\mathrm{d}z}\frac{\partial}{\partial z}\delta k}_{\text{Transport}}+\underbrace{\sigma_0\frac{\partial}{\partial x}\delta u_G+\tau_0\left(\frac{\partial}{\partial z}\delta u_G+\frac{\partial}{\partial x}\delta w_G\right)+\delta\tau\frac{\mathrm{d}U_0}{\mathrm{d}z}}_{\text{Production}}-\underbrace{\delta\mathscr{E}}_{\text{dissipation}}, \tag{28}$$

where k_0 and δk denote the base-state and perturbation TKE, $\delta\mathscr{E}$ is the dissipation of TKE due to turbulence, and $\sigma_0 = \sigma_{01} - \sigma_{02}$. The functional form of the dissipation term is unknown and must be modelled. Here, we assume it to be linear in δk: $\delta\mathscr{E} = (Re_*^2/Re)\delta k$. This is an approximation (other closure laws will be investigated in detail in future work), and is convenient from a mathematical point of view: in this form, the dissipation rate is well-behaved in the dynamically-important interfacial zone, unlike other models (Townsend, 1972, 1980; Ierley and Miles, 2001; Biberg, 2007) that fail to resolve this zone, and possess logarithmic singularities.

We substitute $(\delta u_G, \delta w_G) = (\partial\phi_G/\partial z, -\partial\phi_G/\partial x) \propto e^{i\alpha(x-ct)}$, where subscript G denotes gas-phase quantities, along with $(\delta k, \delta\tau)(x,z,t) \propto e^{i\alpha(x-ct)}$ into Eq. (28), and allow molecular viscosity to dominate its turbulent counterpart in the interfacial region where the latter is negligible (Townsend, 1972, 1980; Ierley and Miles, 2001). Thus, Eq. (28) reduces to the following:

$$\left[i\alpha(U_0-c)+\frac{Re_*^2}{Re}\right]\delta k=\frac{1}{Re}(D^2-\alpha^2)\delta k+\delta\tau\frac{\mathrm{d}U_0}{\mathrm{d}z}+\tau_0(D^2+\alpha^2)\phi+\mathrm{i}\alpha\sigma_0 D\phi_G+i\alpha\frac{\mathrm{d}k_0}{\mathrm{d}z}\phi_G. \tag{29a}$$

The 'visco-elastic' aspect of the model comes from the manner in which the unknown stress $\delta\tau$ is constituted. Such models have been used by Townsend (1972, 1980), and by Ierley and Miles (2001). The model described here fits into the framework of the latter paper, with slight modifications: the base-state quantities are computed according to the formalism in the previous section. Thus, to close the system, the following constitutive relations are posed:

$$\delta\tau-\frac{\tau_0}{k_0}\delta k=0,\quad \delta\sigma-\frac{\sigma_0}{k_0}\delta k=0, \tag{29b}$$

with the base-state stress, τ_0, given by Eq. (8), and σ_0 set equal to the base-state kinetic energy: $\sigma_0 = k_0$; the latter is consistent with the DNS results of Spalart (1988). (29b) are consistent with the statement that the tensor $T_{ij}^{(t)}/k$ maintains its equilibrium (base-state) value (Ierley and Miles, 2001; Pope, 2000).

Finally, the base-state turbulent kinetic energy must be modelled. Instead of writing down a transport equation for the base-state kinetic energy, and invoking a closure assumption for the base-state dissipation, we use the following model:

$$\tilde{k}_0=\frac{k_0}{\rho_G U_p^2}=\frac{1}{C^2}\frac{Re_*^2}{Re^2}\psi(\tilde{z})\psi(1-\tilde{z}), \tag{29c}$$

where C is a constant, here taken to be 0.55, which is the value appropriate for the logarithmic region of the mean velocity in a boundary layer. This form is desirable because it captures both the log-layer behaviour of the turbulent kinetic energy, and the asymptotic behaviour near the upper channel wall and near the interface: for instance, $\tilde{k}_0 \sim \tilde{z}^2$ as $\tilde{z} \to 0$.

3.3. The zero-equation model

In the formalism associated with the so-called 'zero-equation' model, the stresses $\delta\sigma$ and $\delta\tau$ are not related directly to the TKE. Rather, the normal stresses are set to zero, $\delta\sigma = 0$, and the shear stress is modelled as

$$\delta\tau = \mu_T(D^2+\alpha^2)\phi_G, \tag{30a}$$

where

$$\mu_T=\frac{\kappa Re_*}{\sqrt{|R|Re}}G(\tilde{z})\psi_{\mathrm{i}}(\tilde{z})\psi_{\mathrm{w}}(1-\tilde{z}), \tag{30b}$$

viz. Eq. (8). This is a rather basic model of the eddy viscosity, although Belcher and co-workers (Belcher and Hunt, 1993, 1998; Belcher et al., 1994) have used a similar model to Eqs. (30), with the aim of capturing the physics of the equilibrium turbulence.

3.4. Interfacial conditions

To close Eqs. (27), continuity of velocity and tangential stress is imposed at the interface $z = 0$, while the jump condition in the normal stress is also applied. These are standard conditions (Chandrasekhar, 1961), with slight modification for the presence of turbulent stresses, $\delta\sigma$ and $\delta\tau$, on the gas side:

$$\phi_L = \phi_G, \tag{31a}$$

$$D\phi_L = D\phi_G+\frac{\phi_G}{c-U_0}\left[U_0'(0^+)-U_0'(0^-)\right], \tag{31b}$$

$$m(D^2+\alpha^2)\phi_L=(D^2+\alpha^2)\phi_G+\delta\tau_G-\frac{\phi_G}{c-U_0}\sigma_0, \tag{31c}$$

$$\begin{aligned}&m\left(D^3\phi_L-3\alpha^2D\phi_L\right)+\mathrm{i}\alpha rRe(c-U_0)D\phi_L+i\alpha rRe\ U_0'(0^-)\phi_L\\&-\frac{\mathrm{i}\alpha rRe}{c-U_0}(Fr+\alpha^2S)\phi_L\\&=\left(D^3\phi_G-3\alpha^2D\phi_G\right)+\mathrm{i}\alpha Re(c-U_0)D\phi_G+i\alpha Re\ U_0'(0^+)\phi_G\\&+\mathrm{i}\alpha\delta\sigma+D\delta\tau.\end{aligned} \tag{31d}$$

where Fr and S correspond to the Froude and inverse Weber numbers, respectively:

$$Fr=\frac{gh}{(\mu_G/\rho_G h)^2}\frac{r-1}{Re^2},\qquad S=\frac{\sigma}{\mu_G^2/\rho_G h}\frac{1}{Re^2}. \tag{32}$$

Next, the no-slip conditions are applied at $z = -\delta$ and $z = 1$:

$$\phi_L(-\delta)=D\phi_L(-\delta)=\phi_G(1)=D\phi_G(1)=0,$$

and, when the 'visco-elastic' model is used, the following conditions are applied to the TKE:

$$\delta k(0,1)=0. \tag{33}$$

Note that if the 'visco-elastic' model is adopted then $(\delta\sigma,\delta\tau)\sim\delta k$ so $(\delta\sigma,\delta\tau)\to 0$ as $z\to(0,1)$ since $\delta k\to 0$ in these limits; this is also true for the 'zero-equation' model since, in that case, $\delta\sigma = 0$ identically, and $\delta\tau\sim\mu_T\to 0$ as $z\to(0,1)$ since $(G,\psi_i,\psi_w)\to 0$ in these limits. Thus, the turbulent stress contributions in Eqs. (31c) and (31d) vanish leaving the 'standard' interfacial conditions unaltered. The vanishing of these terms occurs only because we have carefully formulated the assumptions concerning the turbulent base state,

highlighting yet again the importance of modelling the flat-interface state accurately. The Orr–Sommerfeld (27b) and the turbulence models reduce to an eigenvalue problem in the eigenvalue c. This is solved numerically according to a standard method, described and validated elsewhere by the current authors in the context of absolute and convective instabilities in laminar two-phase flows (Valluri et al., 2010; Ó Náraigh and Spelt, 2010).

4. Results

In this section, we begin by examining the validity of certain simplifying assumptions that involve the neglect of the turbulent stresses in the linear stability analysis; this is followed by a brief study of the effect of varying Re on the stability characteristics and the establishment of a critical Re which will form the basis for comparisons with experiments. In the remainder of the section, we perform an energy-budget decomposition to identify the dominant mechanism for instability, and investigate the possibility of mode competition. Finally, we assess the possibility that mode competition can be generated by large amounts of interfacial roughness.

4.1. Quasi-laminar hypothesis

Here, we compare the predictions of the turbulence models of the perturbed turbulent stresses against the so-called *quasi-laminar hypothesis*. This hypothesis states that the turbulence makes itself felt primarily through the base state and, consequently, that the perturbed turbulent stresses are to be ignored. We demonstrate that this approximation is sufficient to capture the dominant features and essential physics of the interfacial instability. To do so, we carry out a stability analysis based on the values in Table 1, with $d_L = 2.5$ mm and $\delta = 0.05$. The inverse Froude and inverse Weber numbers are computed as

$$Fr = (3.7809 \times 10^6)\frac{r-1}{Re^2}, \quad S = \frac{1.1420 \times 10^7}{Re^2}. \tag{34}$$

We select a Reynolds number, Re, that produces substantial shear in the liquid, but is such that the liquid remains laminar. Thus, $Re = 1000$, and $Re_L = \tau_i d_L/\mu_L \approx 460$. (We verify *a posteriori* that the liquid remains laminar, in the sense that no unstable modes associated with the liquid exhibit positive growth.)

In Fig. 8, we obtain dispersion curves, describing the dependence of the growth rate $\lambda_r = \alpha c_i$ on the wavenumber α using three models: the basic Orr–Sommerfeld equation without the perturbed turbulent stresses (i.e. the quasi-laminar approach), the visco-elastic model (29), and the zero-equation model (30b), to which we refer below as the 'eddy-viscosity model'. Over a large range of Reynolds numbers ($Re = 500$—5000, $Re_{U_{max}} = \rho_G U_{max} h/\mu_G = 10^3 - -10^5$), the growth rates for the different models differ only quantitatively. In particular, the differences between the quasi-laminar calculation and the eddy-viscosity one are small: the shift

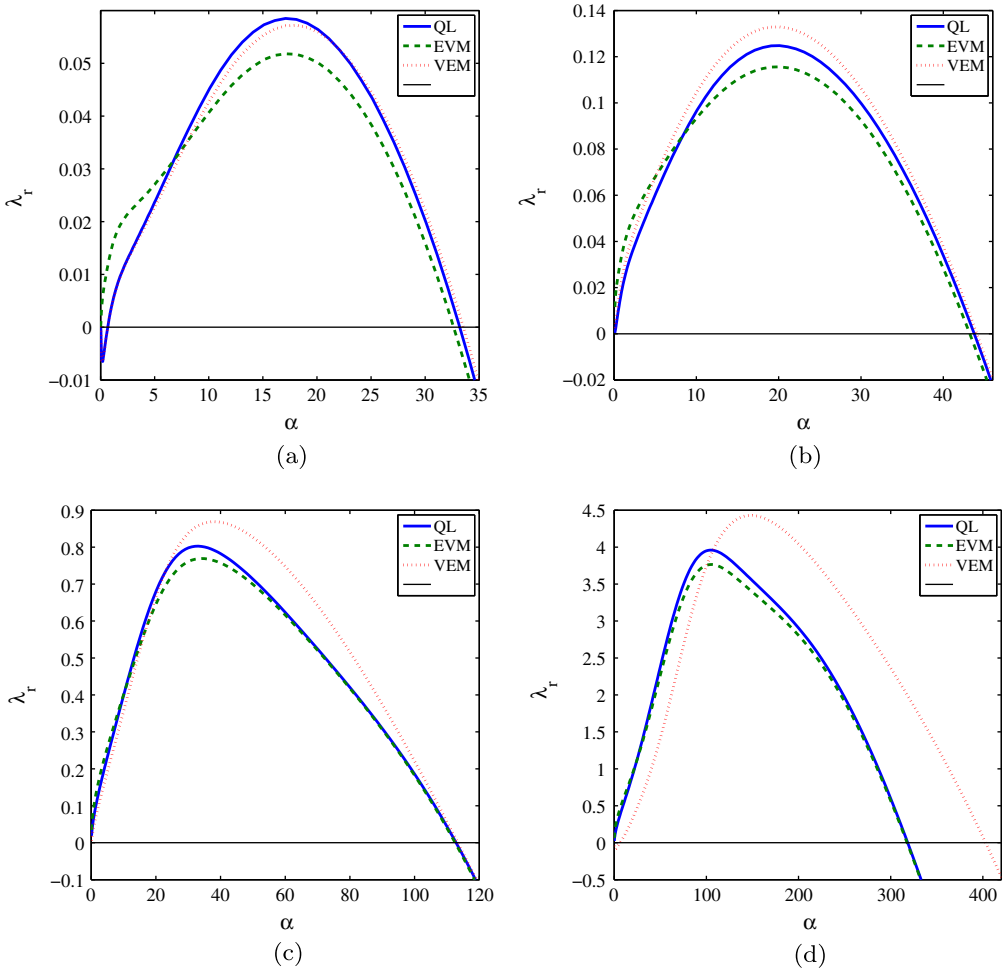

Fig. 8. Dispersion curves showing a comparison of the predictions of the various models described in the text: quasi-laminar model (thick solid lines), eddy-viscosity model (dashed lines), 'visco-elastic' model (dotted lines), denoted by 'QL', 'EVM' and 'VEM' in the panel legends; the horizontal solid lines correspond to zero growth rate. Also shown is the parametric dependence of the growth rate on the Reynolds number for (a) $Re = 875$; (b) $Re = 1000$; (c) $Re = 2000$; (d) $Re = 5000$. We have set $m = 55$, $r = 1000$, and $\delta = 0.05$.

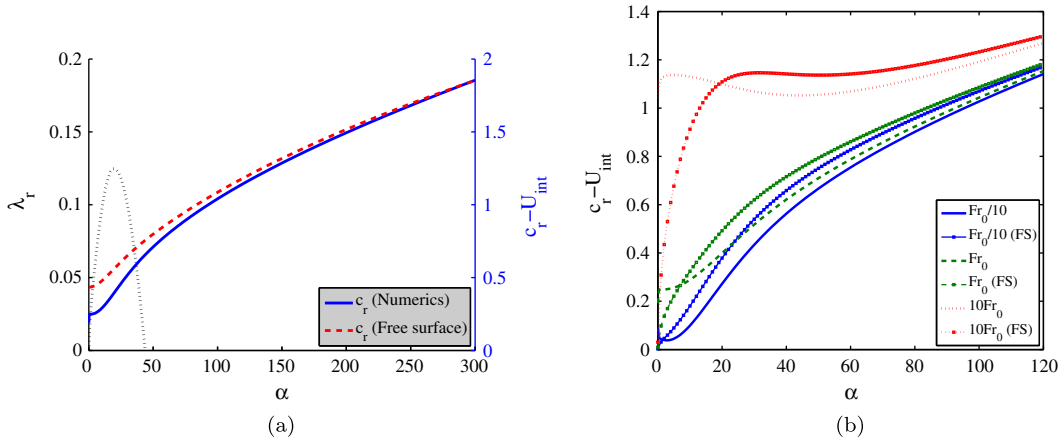

Fig. 9. A comparison of the wave speed c_r computed as part of the solution of the eigenvalue problem with the predictions of Eq. (24) for free-surface waves. In panel (a), the same parameters were used as those in Fig. 8b, while in panel (b), the comparison is shown over a range of Fr at fixed Reynolds number $Re = 1000$. (Fr_0 is the reference value given by Eq. (34).) Also shown in (a) is the dispersion curve from Fig. 8b in dotted lines.

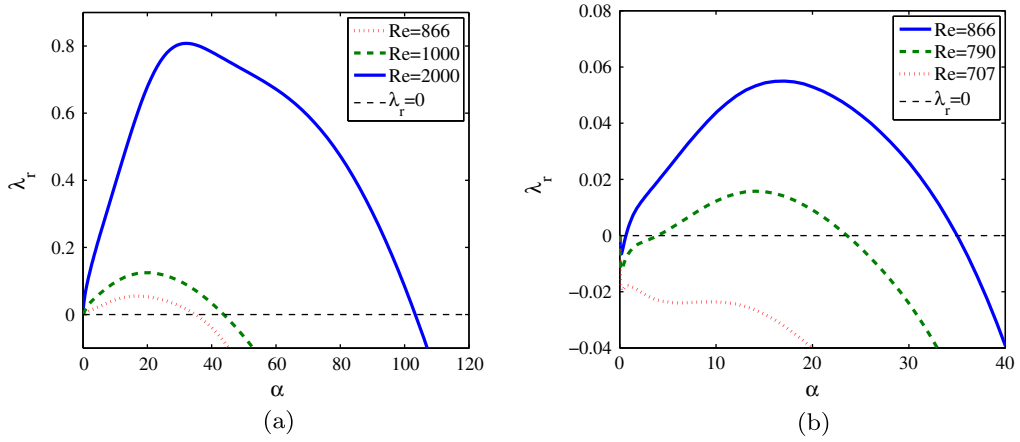

Fig. 10. The effects of varying Re on the dispersion curves using the quasi-laminar assumption. We have set $(m,r,\delta) = (55,1000,0.05)$; Fr and S are given by Eq. (34).

in the maximum growth rate upon including the perturbed turbulent stresses is less than 10% in the cases considered here, while the cutoff wavenumbers are virtually unchanged. The differences between the quasi-laminar calculation and the visco-elastic calculation are slightly larger, increasing with Re. In particular, the cutoff wavenumber is shifted to a higher value in the $Re = 5000$ case (Fig. 8d). Nevertheless, the shift in the maximum growth rate upon including the terms associated with the visco-elastic model is a little over 10% for the largest Re considered in Fig. 8. The minor discrepancy in behaviour between the visco-elastic model and the other two models is due to the simplicity in modelling the kinetic-energy dissipation function, here assigned the simple linear form $(Re_*^2/Re)\delta k$. Accurate modelling of this term will be the subject of future work.

Our conclusion from the small differences evinced by these comparisons is that we are justified in considering the quasi-laminar approximation for the rest of this work. Physically, the marginality of the perturbed turbulent stresses is explained as follows. Any difference in the stability results between the models is driven by the presence of extra terms in the perturbation equations for the bulk flow, and by the existence of extra terms in the interfacial conditions. In our case, the additional terms in the bulk equations scale as $\kappa Re_*/Re$, which for thin layers is approximately $\kappa/\sqrt{2}$, and thus has a small effect. Moreover, in our case, the additional interfacial terms are turbulent in nature, and are thus

Table 2
Energy budget for the most dangerous mode $\alpha = 20$ at $Re = 1000$ (hence $Re_L \approx 460$). Here $m = 55$, $r = 1000$, and $\delta = 0.05$; Fr and S are given by Eq. (34).

KIN_G	KIN_L	REY_L	REY_G	$DISS_L$	$DISS_G$	NOR	TAN
0.18	0.82	2.34	−11.90	−4.28	−57.42	−2.73	74.99

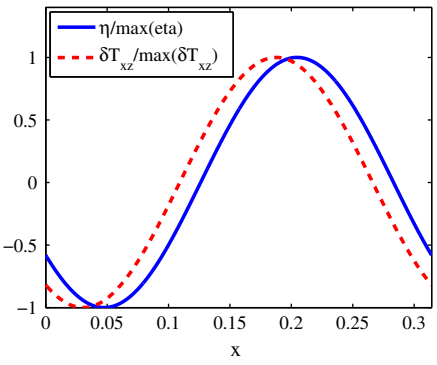

Fig. 11. The phase shift between the viscous shear stress at the interface, $\delta T_{G,xz}$, and the perturbed interface location $\eta(x)$ for the most dangerous mode $\alpha = 20$. The parameters have the same values as those in Table 2.

damped to zero in the viscous sublayer, and vanish at $z = 0$. Hence, this second contribution to the modified growth rate is identically zero. Thus, in the case of equilibrium turbulence considered here, the effects of turbulence are felt almost entirely through the choice of base state. The only possibility for the effects of turbulence to enter through the perturbed turbulent stresses is when the critical-layer instability is present, in which case the perturbed turbulent stresses and the critical layer may interact. However, the discussion of 'slow' and 'fast' waves in Section 2.3 suggests that thin-layer waves are 'slow', and, therefore, not susceptible to the critical-layer instability. In conclusion, we are satisfied that the perturbed turbulent stresses are of marginal importance; therefore, for the rest of the paper, we focus only on the quasi-laminar model.

Finally, in Fig. 9, we investigate the extent to which the wave speed c_r agrees with the free-surface formula (24). Inspection of panel (a) of this figure suggests that the agreement is good in the limit of large α, deteriorating with decreasing α, although it remains a useful order-of-magnitude estimate (for which it is used here). Fig. 9b also shows that the agreement is reasonable over a range of Fr values.

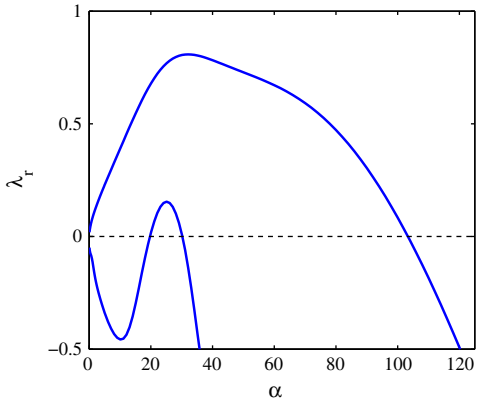

Fig. 12. The appearance of two unstable modes for sufficiently large Re, $Re = 2000$. Here $(m, r, \delta) = (55, 1000, 0.05)$, and Fr and S are given by Eq. (34).

Table 3
Energy budget of the two unstable modes shown in Fig. 12 at $\alpha = 25$. Here we have set $(m, r, \delta, Re) = (55, 1000, 0.05, 2000)$; Fr and S are given by Eq. (34).

α	λ_{max}	KIN_G	KIN_L	REY_L	REY_G	$DISS_L$	$DISS_G$	NOR	TAN
25	0.77	0.85	0.15	0.45	−9.57	−0.41	−36.96	−1.17	48.67
25	0.15	0.15	0.85	3.80	−9.98	−0.80	−26.46	−0.18	34.62

4.2. The critical Reynolds number

We investigate the effect of varying Re on the structure of the dispersion curves, using the quasi-laminar assumption; emphasis is placed on the variation of the cutoff wavenumber and maximum growth rate with Re. The results shown in Fig. 10 demonstrate that the maximum growth rate increases monotonically with Re. Furthermore, upon decreasing Re, the lower critical wavenumber shifts from $\alpha_{cl} = 0$ to a finite value $\alpha_{cl} > 0$, suggesting that for a given parameter set $(m, r, \delta, Re^2, S, Fr)$, there is a critical Reynolds number for stability. This is exemplified by Fig. 10, where the critical Reynolds number is $Re_c \approx 750$. The existence of the critical Reynolds number provides a means of comparing our models with experiments (Section 5). First, however, we examine some further properties of the eigenvalue problem, which characterises the quasi-laminar model.

4.3. Energy-budget decomposition and identification of unstable modes

In this subsection, we use an energy budget to classify the instabilities observed. The linearised dynamical equations associated with the Orr–Sommerfeld equations possess an energy

$$\underbrace{\frac{1}{2}\int_{-\delta}^{0} dz \int_{0}^{2\pi/\alpha} dx |\delta \boldsymbol{u}_L|^2}_{=E_L} + \underbrace{\frac{1}{2}\int_{0}^{1} dz \int_{0}^{2\pi/\alpha} dx |\delta \boldsymbol{u}_G|^2}_{=E_G},$$

where $r_L = r$ and $r_G = 1$, which grows or decays in time according to the stability of the base state. By matching the time change in the kinetic energy $KIN_j = dE_j/dt (j = G, L)$ with the inputs of power into the perturbations, an energy budget is obtained (Hooper and Boyd, 1983; Kelly and Goussis, 1989; Boomkamp and Miesen, 1996):

$$KIN_G + KIN_L = DISS_G + DISS_L + REY_G + REY_L + NOR + TAN,$$

where $DISS_{G,L}$ denotes energy loss through viscous dissipation, $REY_{G,L}$ denotes wave-Reynolds-stress terms that correspond to transfer of energy from the mean flow into the perturbations in the bulk parts of the two phases; NOR and TAN denote energy delivered by the normal and tangential stresses at the interface. For the quasi-laminar model, the perturbed turbulent stresses, being of marginal importance, are ignored. Of particular interest in the present application are the terms

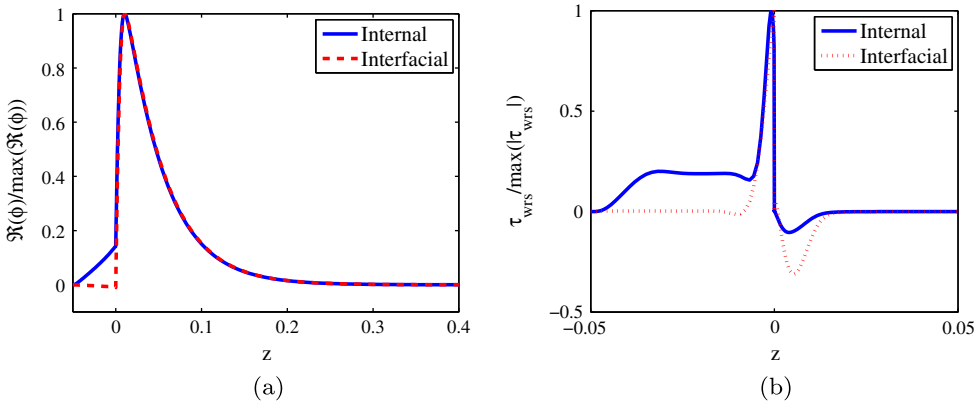

Fig. 13. (a) The streamfunction for the internal and interfacial modes, normalised such that $max|\Re(\phi)| = 1$, for the parameters used to generate Fig. 12 and $\alpha = 25$; (b) the wave Reynolds-stress function for the internal and interfacial modes, τ_{wrs}, normalised such that $\max\tau_{wrs} = 1$.

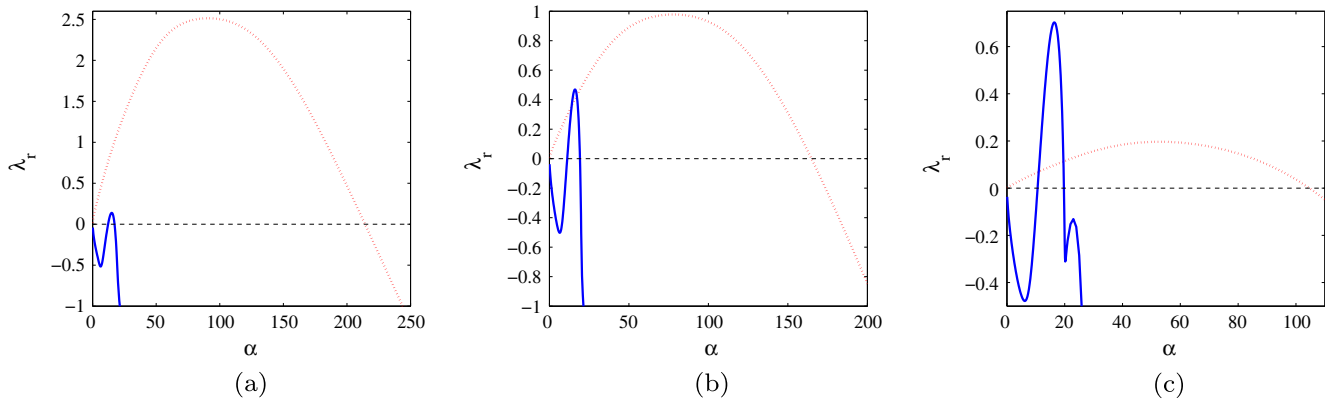

Fig. 14. Dependence of the dispersion curves on the interfacial-roughness parameter, for $K = 0,0.001,0.005$, shown in (a–c), respectively; in each panel the interfacial and internal modes are shown using solid and dashed lines, respectively. Here, we have set $(m,r,\delta,Re) = (55,1000,0.05,4000)$.

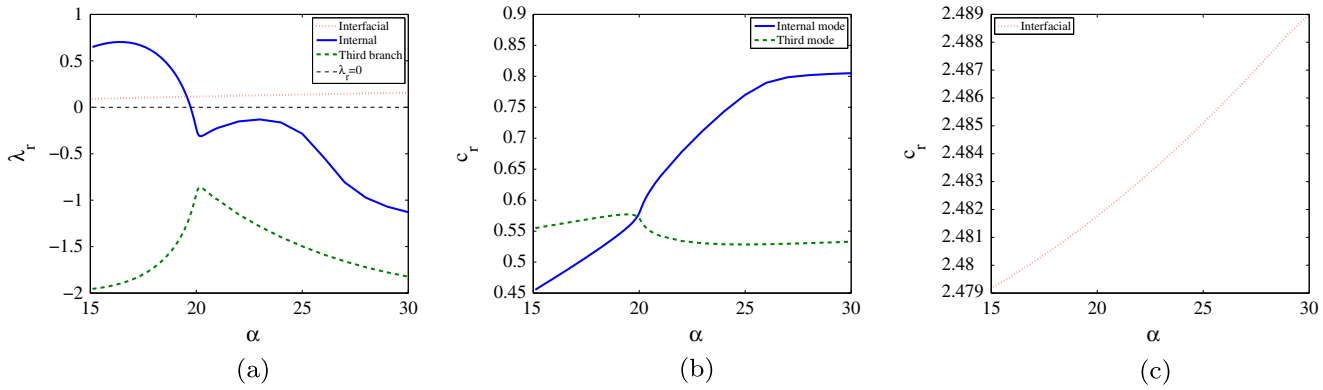

Fig. 15. Companion to Fig. 14(c). (a) The growth rate of the three most dangerous modes at $Re = 4000$ and $K = 0.005$, being an enlarged view of the $\alpha = 15$–30 region of Fig. 14(c). The sharp kink or extreme point in the growth rate of the internal mode is thus genuine, and not the consequence of mode crossover. (b) Furthermore, by examining the wave *speed*, we see that the wave speed of the internal and the third most dangerous modes do in fact cross close to the corresponding extreme point of the growth-rate curves. Finally, (c) shows the wave speed of the interfacial mode.

$$REY_L = \int_{-\delta}^{0} \mathrm{d}z \tau_{L,\mathrm{wrs}}(z) U_0'(z), \quad \tau_{L,\mathrm{wrs}}(z) = -r \int_0^{2\pi/\alpha} \mathrm{d}x \delta u_L \delta w_L, \quad (35)$$

$$REY_G = \int_{0}^{1} \mathrm{d}z \tau_{G,\mathrm{wrs}}(z) U_0'(z), \quad \tau_{G,\mathrm{wrs}}(z) = -\int_0^{2\pi/\alpha} \mathrm{d}x \delta u_G \delta w_G, \quad (36)$$

and

$$TAN = \int_0^{2\pi/\alpha} \mathrm{d}x [(\delta u_L - \delta u_G)\delta T_{G,xz}]_{z=0}, \quad (37)$$

where $\delta T_{G,xz}$ is the off-diagonal component of the viscous stress tensor in the gas layer. Using this decomposition, we characterise the instability in Fig. 9a, for which $m = 55$, $r = 1000$, $\delta = 0.05$, and $Re = 1000$. The most dangerous mode is at $\alpha \approx 20$, which equates to a wavelength $2\pi/\alpha \approx d_L$. The energy budget of this mode is given in Table 2. The results in this table indicate that it is the *TAN* term that is the main source of the instability. To understand this term in more depth, we apply the kinematic condition

$$\delta u_L - \delta u_G = \eta[U_0'(0^+) - U_0'(0^-)] = \eta U_0'(0^-)(m-1), \quad \text{on } z = 0,$$

to the tangential term (37), to obtain

$$TAN = (m-1)\frac{Re_*^2}{Re} \int_0^{2\pi/\alpha} \mathrm{d}x \eta(x) \delta T_{G,xz}(x, z = 0). \quad (38)$$

Thus, $TAN > 0$ is consistent with $m > 1$, provided the phase shift between the interfacial height $\eta(x)$ and the disturbance stress $\delta T_{G,xz}(x, z = 0)$ is small. Specifically, the phase shift must be in the range $\left[-\frac{\pi}{2}, \frac{\pi}{2}\right]$; see Fig. 11. This means that the interface destabilises through the *viscosity-contrast mechanism* (also called the Yih mode (Yih, 1967)). Similar results hold over a range of parameter values $1000 \leqslant Re \leqslant 10{,}000$, $0.1Fr_0 \leqslant Fr \leqslant 10Fr_0$, and $0.1S_0 \leqslant S \leqslant 20S_0$, where (Fr_0, S_0) represent the reference values used in Table 2. This confirms the dominance of the viscosity-contrast mechanism in destabilising the interface in the thin-film case considered.

We now examine a second unstable mode which appears for sufficiently large *Re*; an example of this is shown in Fig. 12 for $Re = 2000$. The energy budget of the two unstable modes is shown in Table 3. The first mode, associated with the eigenvalue branch that has interested us until now, derives all but a small fraction of its destabilising energy from the *TAN* term, which as was mentioned above, owes its existence to work done by the tangential stress on the interface. This term is positive when $m > 1$, and we designate this mode the 'interfacial' mode. The second, less unstable mode derives the majority of its destabilising energy from this source too, although the magnitude of the term REY_L is larger for this mode. Thus, the transfer of energy from the mean flow to the perturbation in the liquid is destabilising. This mode is commonly called the 'internal' one (e.g. Miesen and Boersma, 1995).

Fig. 13a shows the streamfunction for these two modes. The streamfunction of the internal mode possesses a large non-zero component in the liquid, in contrast to that of the interfacial mode. This produces significant flow in the liquid, and hence gives an important contribution to the wave-Reynolds-stress term, REY_L.

Table 4
Comparison of our model predictions with the work of Cohen and Hanratty (1965) (see text for definition of Re_{CH}). The sub-table is an energy-budget decomposition related to experiment (3), with $\alpha = 5.5$; the other parameters are chosen to match those in the experiment.

Experiment	d_L (mm)	Re_{CH}	Re_{CH} (exp)	$c_r/\overline{U}_G$	$c_r/\overline{U}_G$ (exp)	$2\pi/\alpha$ (in.)	$2\pi/\alpha$ (in.,exp)
(1)	1.89	3810	4050	0.13	0.08	1.1	0.9
(2)	3.54	2650	2760	0.15	0.15	0.7	1.2
(3)	4.91	1930	1980	–	0.19	0.9	–

α	KIN_G	KIN_L	REY_L	REY_G	$DISS_L$	$DISS_G$	NOR	TAN
5.5	0.99	0.01	4.58	1.91	−21.32	−31.44	−1.55	48.82

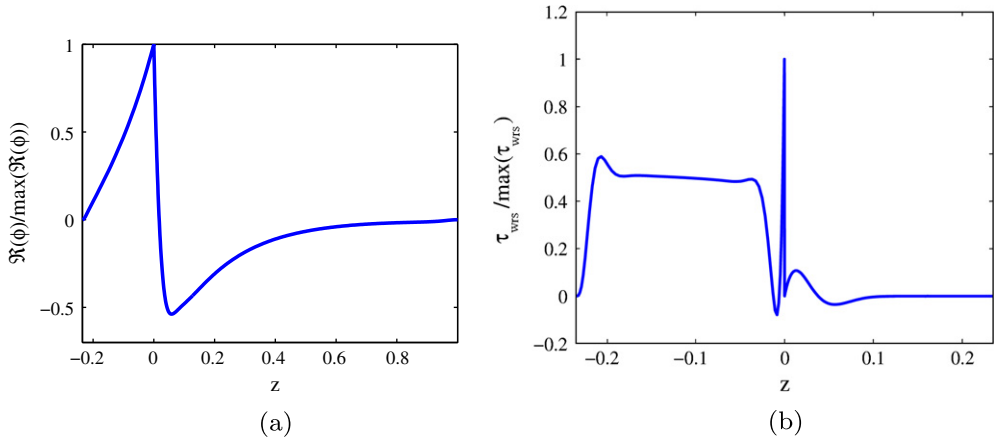

Fig. 16. Theoretical calculation based on the parameters in experiment (5) of Cohen and Hanratty. (a) The streamfunction; (b) the wave-Reynolds stress.

The development of such a term is shown in Fig. 13, where we plot the wave-Reynolds-stress, τ_{wrs} in the liquid and the gas (Eqs. (35) and (36)) for both modes; this function is non-zero throughout the liquid layer in the internal-mode case, confirming the importance of the dynamics in the bulk of the liquid for the development of this less unstable mode.

The existence of a second unstable mode implies the possibility of mode competition, in which the most dangerous mode changes type, from being interfacial to internal. We have verified that this competition can be effected by decreasing m, which decrease the importance of the interfacial mode relative to the internal mode. A similar modal competition has been observed in two-phase mixing layers by Yecko et al. (2002), where the mode competition is also a function of the viscosity contrast. Instead of pursuing this mechanism of competition in detail, we turn instead to the variations in the interfacial roughness, which can also engender modal competition.

4.4. Modelling interfacial roughness

We examine the effect of interfacial roughness on the internal and interfacial modes. We use the model described in Section 2.2, where the eddy-viscosity contains an explicit roughness parameter $K = \ell_i/(\kappa h)$, and where ℓ_i is the mean height of the roughness elements. In view of the success of the quasi-laminar hypothesis in describing the linear stability of smooth base states, its use is extended to the surface-roughened case considered here. Fig. 14 shows the effect of varying the roughness parameter K on the dispersion curves. As K increases, the maximum growth rate of the interfacial mode shrinks dramatically, while the maximum growth rate of the internal mode increases slightly. This change is sufficient to promote the maximum wavenumber-growth-rate pair on the internal branch, $(\alpha_{max,int}, \lambda_{max,int})$, to the status of most dangerous mode. This crossover occurs for $K \gtrsim 0.001$, as shown in Fig. 14b.

In Fig. 14c, the dispersion curve of the internal mode possesses a local minimum near $\alpha \approx 20$. To verify that this is not due to a crossover between the second and third modes, we have plotted the three least negative modes for $K = 0.005$ in Fig. 15a. The second and third least negative modes are well separated and a crossover effect is thus ruled out. Fig. 15b and c is plots of the wave speed for the internal and interfacial modes: the continuity of these curves confirms that no crossover effect is taking place. Note, however, that the wave speeds of the second and third most dangerous modes intersect close to the point where the internal mode has its local minimum. Such phenomena often occur in modal coalescence (Shapiro and Timoshin, 2005). The difference $c_r - U_{int}$ is negative for the internal mode, which shows that the critical layer is in the liquid for the internal mode. Note finally that although the roughness-modified eddy viscosity has been rigorously validated by Biberg (2007), and although (Morland and Saffman, 1993) have explained previously how interfacial roughness can reduce the growth rate of the wave, our interfacial roughness results must be confirmed, ultimately, by experiments or DNS, data which, to

Table 5
Comparison with Table 1 (p. 375) and Table 2 (p. 378) in the work of Craik (1966). The Reynolds number Re_{Cr} is defined with respect to the gas density and viscosity, the channel height, and the interfacial velocity.

Experiment	d_L (mm)	Re_{Cr}	Re_{Cr} (exp)	c_r/U_{int}	c_r/U_{int} (exp)
(1.1)	0.128	20	30		
(1.2)	0.230	68	61		
(1.3)	0.218	66	71		
(1.4)	0.355	110	140		
(1.5)	0.307	94	140		
(2.1)	0.535	35	94	1.1	1.75
(2.2)	0.665	50	89	1.0	1.9
(2.3)	0.820	56	91	1.1	1.8

Table 6
Theoretical energy-budget calculations related to experiments (1.5) and (2.1) of Craik (1966). The instability is viscosity-induced, and there are no other contributions to the instability, unlike in the Cohen data.

	α	KIN_G	KIN_L	REY_L	REY_G	$DISS_L$	$DISS_G$	NOR	TAN
(1.5)	0.3	1.00	0.00	0.00	−165.56	−2.47	−1359.25	−0.09	1528.37
(2.1)	0.02	1.00	0.00	0.00	−45.06	−3.23	−701.34	−0.14	750.76

our knowledge, are not yet available. In the next section we turn to an aspect of our investigations for which experimental data are available, namely the thin-layer, flat-interface base state.

5. Comparison with experiments and other models

We compare our results with some of the experimental data from the literature, in particular the work of Cohen and Hanratty (1965) and Craik (1966). We also compare our findings with a model that is frequently used in practical applications to predict flow-regime transitions, namely the 'viscous' Kelvin–Helmholtz theory.

5.1. Comparison with experiments

Cohen and Hanratty (1965) report critical Reynolds numbers for millimetre-thick water films forced by air. They observe the development of two-dimensional waves above a critical Reynolds number. They call these waves 'fast', in the sense they move at a velocity that exceeds the interfacial velocity. These waves are, however, in our classification, 'slow' (or on the boundary between 'slow' and 'fast'), since the theoretical values computed are $c_r/U_p \gtrsim 1$, and thus the viscosity-contrast instability is expected. We show a comparison between the theoretical predictions of our model and the measurements of Cohen and Hanratty in Table 4. Our estimates for the critical Reynolds number $Re_{CH} = \rho_G h\overline{U}_G/\mu_G$ are in close agreement with the experimental values, well within the margin of error in the experiments, reported to be in the range of 10–20%. We have also compared our theoretical model with the measurements of the critical wavelength and wave speed. There is reasonable agreement between the theoretical and experimental values for the wave speed. The spread in values of the critical wavelength is larger, although this is acceptable, in view of the large error attached to the experimental measurements. The energy budget in Table 4 is based on a calculation, with parameters taken from experiment (3). Specifically, $Re = 207.3$, $r = 873.9$, $m = 50.45$, $\delta = 0.2350$, $Fr = 346{,}100$, $S = 5{,}258{,}000$. The corresponding streamfunction and the wave-Reynolds stress function are presented in Fig. 16. The instability is confirmed to be due to the viscosity-contrast mechanism, with additional, inertial contributions from the liquid and gas phases.

Craik (1966) performs a similar experiment with liquid films thinner than those found in Cohen and Hanratty (1965) and reports critical conditions for instability. The trend in the data in Table 5 agrees with that in our calculations, although the quantitative agreement deteriorates with increasing film thickness (see sub-table containing runs (2.1)–(2.3); we do not compare our results with runs (2.4) and (2.5) in Craik (1966) wherein our model predicts laminar gas flow). Craik explains that waves are observed for film thickness below that quoted in experiment (1.1), although the uniform thin film of liquid is difficult to maintain under these conditions. It is possible that the thinness of the film inhibits precision in the measurement at film thickness above this lower bound too. Craik also explains that accurate measurements of wave speed were difficult owing to the long wavelengths of the observed waves (compared to the channel length). These are sources of error that explain why there is only qualitative agreement between the theoretical and experimental data. Finally, the energy budget in Table 6 is based on a theoretical calculation, with parameters taken from experiments (1.5) and (2.1). The instability is controlled entirely by the viscosity-contrast mechanism; the contributions from the bulk phases seen in the previous case (Tables 4 and 5) are absent here, since the liquid film is much thinner.

5.2. Comparison with 'viscous' Kelvin–Helmholtz theory

In this section, we compare our predictions with those obtained using viscous Kelvin–Helmholtz theory (Barnea, 1991). This is a simplified theory for the interfacial instability of two-phase turbulent flow, and takes account of turbulence in either or both phases. It is commonly used in one-dimensional models for large-scale stratified and slug-flow predictions. The velocity field enters only through the liquid- and gas-averaged values, u_L and u_G, while the cross-sectional area fractions $\epsilon_L = d_L/(d_L + d_G)$ and $\epsilon_G = d_G/(d_L + d_G)$ also play a role. Then, the complex frequency ω is obtainable from a quadratic equation, the details of which can be found in Appendix B.

We plot the stability boundary predicted by this theory in Fig. 17, and compare the results with Craik's data for experiment-set 1 (a 6-in. channel) (Table 5), and with a curve fit based on a number of points obtained from our calculations. The viscous Kelvin–Helmholtz model overpredicts the critical Reynolds number compared with both the data of Craik (1966) and our theoretical model by an order of magnitude (Fig. 17). This casts severe doubts on the usefulness of such a depth-averaged model. Our model gives better agreement with the data of Craik (1966), although we are mindful of the experimental error associated with these data. Nevertheless, both our theoretical calculations and the experimental data demonstrate the unstable–stable–unstable transition that arises when the film depth is increased, holding the Reynolds number fixed. This is the statement that our theoretical curve in Fig. 17 is non-monotonic (the non-monotonicity in the

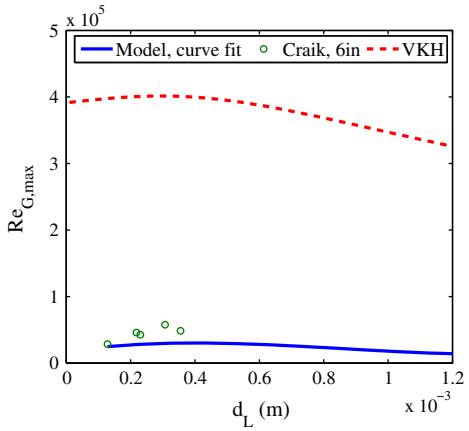

Fig. 17. A comparison of our predictions with the 'viscous' Kelvin–Helmholtz model (see (B) for details), labelled 'VKH', and the experimental data of Craik (1966). We have plotted the Reynolds number $Re_{G\max} = \rho_G U_{G\max} d_G/\mu_G$ against the liquid film thickness d_L.

model curve is masked somewhat by the large scale necessary to show the viscous Kelvin–Helmholtz results in the same figure).

In conclusion, the model predictions of the critical Reynolds number agree reasonably well with experiments, and inspire confidence in our base-state formulation. To obtain this agreement, no parameter tuning was required: we simply backed out the pressure drop from the experimental papers and used our model for these cases. This is in contrast to (for example) the work of Miesen and Boersma (1995), wherein the authors encountered some difficulty in matching up the model parameters with the experimental conditions. Furthermore, the poor agreement between the predictions of the viscous Kelvin–Helmholtz theory and experimental data (and our model predictions) calls into question the validity of this depth-averaged model, at least for the kind of thin-film waves studied here.

6. Conclusions

In this paper, we have investigated the linear stability of an initially flat interface separating a thin, primarily laminar liquid layer (although cases wherein this layer is turbulent are also considered briefly) from a turbulent gas in a rectangular channel. A base-state model for the flow is derived, which is a generalisation of the model of Biberg (2007). In this model, both phases are assumed to be steady and fully-developed, and a modified mixing-length theory is employed in which an interpolation function is used for the eddy viscosity; this function is capable of reproducing the 'law of the wall' near the gas–liquid and gas–solid interfaces. The model also employs standard van Driest functions that damp the effects of turbulence as these interfaces are approached. This model has also been extended to include effects of interfacial roughness, which may be brought about physically by pressure fluctuations in the turbulent phase. Crucially, the model does not contain any 'adjustable' or 'fitting' parameters. Yet, in spite of this feature, the predictions of this model are in excellent agreement with the results of experimental data as well as direct numerical simulations. This is one of the two main achievements of this paper (the other, related to linear stability, will be summarised below): to the best of our knowledge, no such base-state model exists in the literature.

In order to investigate the linear stability of the base state, we have started from the linearised Reynolds-averaged Navier–Stokes equations in the turbulent phase, and the linearised Navier–Stokes equations in the laminar phase. We then considered different models for the perturbed turbulent stresses: one in which these stresses are directly related to the turbulent kinetic energy, and another in which they are related to the turbulent velocity field with a simple eddy-viscosity model. In both cases, the perturbed turbulent stresses are damped to zero at the gas–liquid interface.

The linear stability of smooth interfaces was then examined via numerical solution of the linearised eigenvalue equations, which correspond to a generalised Orr–Sommerfeld problem. The effects of the perturbed turbulent stresses on the linear stability were shown to be negligibly small. This is the second main finding of this paper: the influence of perturbed turbulent stresses on interfacial instabilities had been an unresolved issue in the literature prior to the present work. On the basis of these findings, the remaining results in the paper were generated in the 'quasi-laminar' hypothesis according to which the turbulence enters the problem through the base state only.

A decomposition of the energy associated with the most dangerous mode was also carried out, which revealed that, in the majority of the cases considered, the interface is destabilised as a result of a viscosity mismatch; this gives rise to 'interfacial' modes. Cases wherein additional, 'internal' Tollmien–Schlichting-type modes are also destabilised have also been studied; in these cases, the 'internal' modes are sub-dominant to the 'interfacial' modes. Competition between these modes was demonstrated only for the case where significant interfacial roughness is considered. It is hoped that the latter result can lead to experimental work aimed at validating our predictions.

Acknowledgements

This work has been undertaken within the Joint Project on Transient Multiphase Flows and Flow Assurance. The Authors wish to acknowledge the contributions made to this project by the UK Engineering and Physical Sciences Research Council (EPSRC) and the following: – Advantica; BP Exploration; CD-adapco; Chevron; ConocoPhillips; ENI; ExxonMobil; FEESA; IFP; Institutt for Energiteknikk; PDVSA (INTEVEP); Petrobras; PETRONAS; Scandpower PT; Shell; SINTEF; StatoilHydro and TOTAL. The Authors wish to express their sincere gratitude for this support.

Appendix A. Further validation of the base state

For further validation of the base state discussed in Section 2, we compare our turbulence modelling with the numerical simulations of Adjoua and Magnaudet (2009), and the experiments of Zilker et al. (1976) and Abrams and Hanratty (1985). First, we consider the work of Adjoua and Magnaudet (2009). This involves a large-eddy simulation (LES) of an air–water system where the bottom layer (a thin film of water) is laminar. A pressure gradient drives the turbulence in the gas, and is absent in the liquid. A symmetry condition is imposed at the gas boundary: thus, the geometry of the system is identical to that described by Solbakken and Andersson (2004). The liquid Reynolds number, based on the film height and film superficial velocity, is $Re_L = 4$. The gas Reynolds number, based on the interfacial friction velocity and the gas-layer depth, is $Re_{*,G} = 500$. To agree with our model, we choose Re_0 such that $Re_{*,G} = 1000$; this is twice the value given in the numerical study because we solve for the flow in the entire domain. The results of this calculation are shown in Fig. 18. The agreement between the LES data and our model is good: our model reproduces the logarithmic layer and the viscous sublayer accurately. These features are captured well but not perfectly in the data; this could be due to an excessively large filter width in the LES. Nevertheless, the agreement is good, in particular in the dynamically important viscous and buffer layers. Furthermore, a key assumption of our model is validated by the LES data of Adjoua and Magnaudet (2009). Namely, and on average, the upper layer 'sees' the bottom layer, which is much denser and more viscous, as a solid wall moving at the mean interfacial velocity.

Next, we compare our turbulence modelling with experimental data for flow past a wavy wall, obtained from the papers of Zilker et al. (1976) and Abrams and Hanratty (1985). In this set of experiments, the amplitude a of the corrugation of the lower wall is finite, but the slope αa is assumed infinitesimal. The curvilinear coordinates necessary in such a scenario were first introduced by Benjamin (1958)[1]:

$$\xi = x - ia\Phi,$$
$$\eta = z - a\Phi, \quad \Phi = e^{-\alpha z}e^{i\alpha x}. \tag{A.1}$$

If the streamfunction has the form

$$\phi = \int_0^\eta U_0(s)\mathrm{d}s + aF(\eta)e^{i\alpha\xi}$$

(where U_0 is the single-phase version of the base state in Eq. (14)), then the momentum-balance equation for F is

[1] We thank S. Kalliadasis and D. Tseluiko for suggesting the application of this coordinate system to the problem.

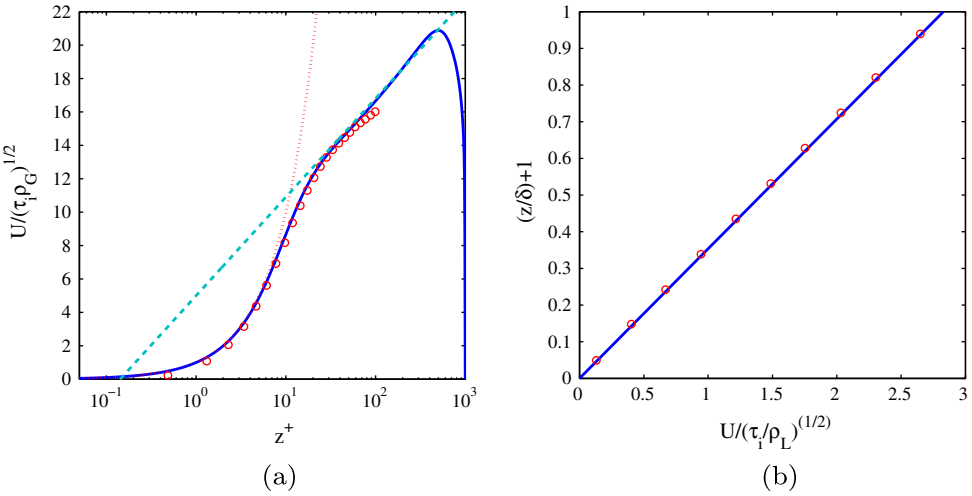

Fig. 18. Comparison with the results of Adjoua and Magnaudet (2009). (a) The mean profile with the viscous-sublayer and log-layer laws for comparison. Our model possesses both these features; the LES data approximates these features but does not capture them perfectly. (b) The liquid profile. The liquid is laminar and experiences no pressure gradient.

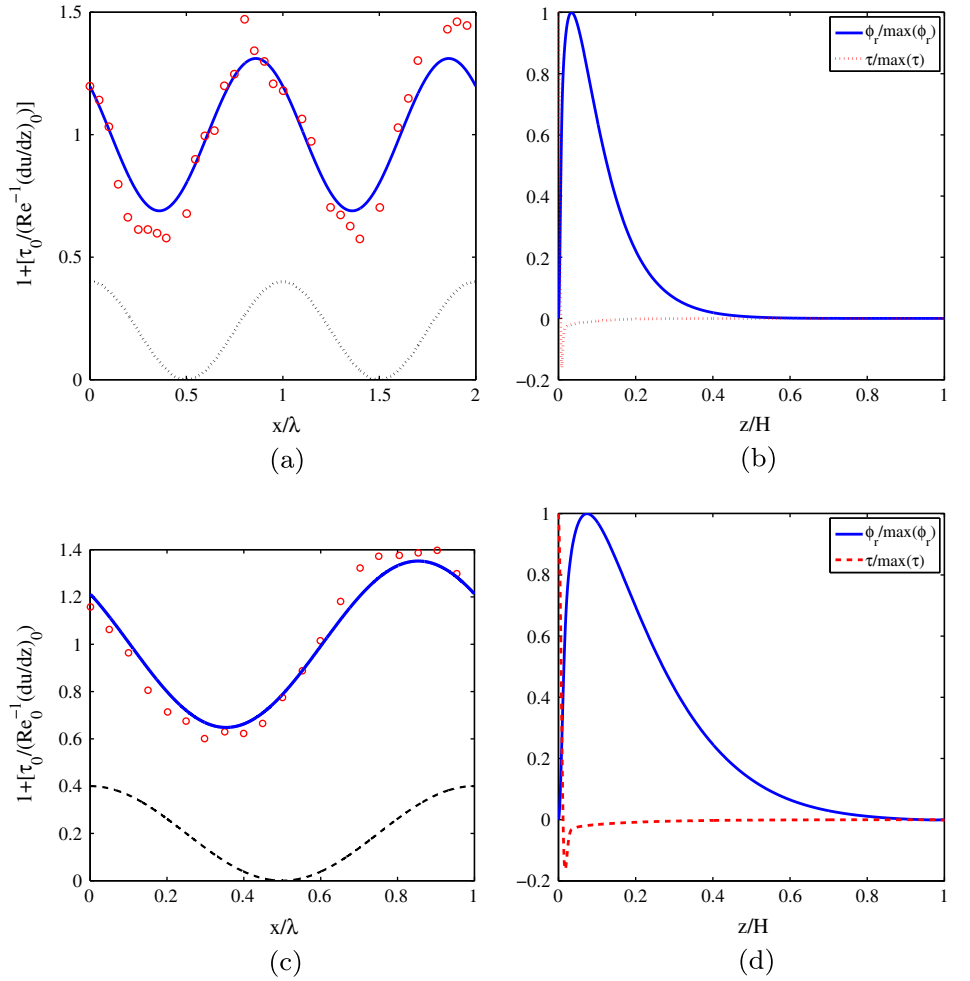

Fig. 19. Comparison with experiments for flow past a wavy wall. Figures (a) and (b) are for the data of Zilker et al. (1976) (Eq. (A.4)); figures (c) and (d) are for the data of Abrams and Hanratty (1985) (Eq. (A.5)).

$$i\alpha\left[\left(\partial_\eta^2-\alpha^2\right)F(\eta)-U_0''(\eta)F(\eta)\right]+\mathscr{C}=\frac{1}{Re}\left(\partial_\eta^2-\alpha^2\right)^2F(\eta)+\mathscr{R}, \tag{A.2a}$$

where $\mathscr{C}$ is the curvature-related term

$$\mathscr{C}=2i\alpha^2U_0'(\eta)U_0(\eta)e^{-\alpha\eta}+\frac{1}{Re}e^{-\alpha\eta}\left[4\alpha^2U_0''(\eta)-2\alpha U_0'''(\eta)\right], \tag{A.2b}$$

and $\mathscr{R}$ is the Reynolds-stress term:

$$\mathscr{R} = 2e^{-\alpha\eta}\left[\alpha\tau_0''(\eta) - \alpha^2\tau_0'(\eta)\right], \quad \tau_0(\eta) = \mu_T(\eta)U_0'(\eta), \tag{A.2c}$$

where we work with the quasi-laminar approximation. We solve Eqs. (A.2) subject to the boundary conditions $F = F' = 0$ on $\eta = 0$ and on $\eta = 1$, which are no-slip conditions on the perturbation F. Although the no-slip condition on the upper boundary is at $z = 1$, not $\eta = 1$, these planes are close to one another: the physical boundary $z = 1$ corresponds to an η-value $1 - ae^{-\alpha}e^{i\alpha x}$, which is close to unity for large α-values. Thus, for simplicity, we impose a boundary condition at $\eta = 1$.

The solution of the boundary-value problem facilitates a comparison with experimental data. In this comparison, we use the *quasi-laminar assumption*, wherein the turbulence enters only through the shape of the base state U_0. To make an accurate comparison between the experiments and Eqs. (A.2) we study the shear stress at the interface:

$$\begin{aligned}\delta\tau &= Re^{-1}(\phi_{zz} - \phi_{xx})_{\eta=0} \\ &= \frac{ae^{i\alpha\xi}}{Re}\left[F''(0) + \alpha^2 F(0) + 2\alpha\left(Re_*^2/Re\right)\right].\end{aligned} \tag{A.3}$$

We also study the phase shift between this stress function and the wave surface $a\Re[e^{i\alpha\xi}]$. We examine the situation described by Fig. 5 in the work of Zilker et al. (1976), for which

$$a/H = 0.003, \quad \alpha H = 13.3, \quad Re_* = 2270, \tag{A.4}$$

where $H = 5.08$ cm is the channel depth. We also look at Fig. 4 in the work of Abrams and Hanratty (1985), where

$$a/H = 0.007, \quad \alpha H = 2\pi, \quad Re_* = 1110, \tag{A.5}$$

where H is the same is in the Zilker experiment.

A comparison between theory and experiment is shown in Fig. 19. Fig. 19a and b shows the results of a comparison for the experiment described by Eq. (A.4). Fig. 19a is a plot of the total shear stress at the interface,

$$\left[Re^{-1}U_0'(0) + \delta\tau(x)\right] \Big/ \left[Re^{-1}U_0'(0)\right],$$

wherein the theoretical curve is compared with the data from the experiment. Reasonable agreement is obtained for the amplitude. Excellent agreement is obtained for the phase shift of the shear stress relative to the wavy wall: the data predicts a phase shift of approximately 50°, while our model predicts a phase shift 52.6°. The wavy wall is shown in the figure for comparison, albeit with an exaggerated amplitude. The parameter α/Re_* has the value 0.0059, while $a\alpha = 0.04$. Fig. 19b provides theoretical curves for the shape of the streamfunction and the stress distribution $Re^{-1}(\phi_{zz} - \phi_{xx})_{x=x_0}$, where x_0 is some reference value. The plots in Fig. 19c and d are similar; these are for the experiment described by Eq. (A.5).

To conclude, the wavy-wall scenario described here serves as an adequate testbed for verifying the turbulence modelling of our base state. However, it is an incomplete model of two-phase flow, since it assumes that the wave speed is a parameter. For that reason, we have focussed on genuine two-phase flow in the main part of the paper.

Appendix B. Application of the viscous Kelvin–Helmholtz theory

In this section, we review the viscous Kelvin–Helmholtz theory (Barnea, 1991) used in the comparison in Section 5.2. This is a simplified theory for the interfacial instability of two-phase turbulent flow, and takes account of turbulence in either or both phases. It is commonly used in one-dimensional models for large-scale stratified and slug-flow predictions. The velocity field enters only through the liquid- and gas-average values, u_L and u_G, while the cross-sectional area fractions $\epsilon_L = d_L/(d_L + d_G)$ and $\epsilon_G = d_G/(d_L + d_G)$ also play a role. Then, the complex frequency ω is obtainable from a quadratic equation:

$$\omega^2 - 2(x_0\alpha - x_1 i)\omega + (x_2\alpha^2 - x_3\alpha^4 - ix_4\alpha) = 0,$$

where

$$\rho_* = \frac{\rho_L}{\epsilon_L} + \frac{\rho_G}{\epsilon_G},$$

$$x_1 = \frac{1}{\rho_*}\left(\frac{\rho_L u_L}{\epsilon_L} + \frac{\rho_G u_G}{\epsilon_G}\right),$$

$$x_2 = -\frac{S_i}{2\rho_* A}\left(\frac{1}{\epsilon_L} + \frac{1}{\epsilon_G}\right)\left(\frac{1}{\epsilon_G}\frac{\partial\tau_i}{\partial u_G} - \frac{1}{\epsilon_L}\frac{\partial\tau_i}{\partial u_L} + \frac{1}{\epsilon_L}\frac{\partial\tau_{iL}}{\partial u_L} - \frac{1}{\epsilon_G}\frac{\partial\tau_{iL}}{\partial u_G}\right),$$

$$x_3 = \frac{1}{\rho_*}\left[\frac{\rho_L u_L^2}{\epsilon_L} + \frac{\rho_G u_G^2}{\epsilon_G} - g(\rho_L - \rho_G)(d_L + d_G)\right],$$

$$x_4 = \frac{\sigma}{\rho_*}(d_L + d_G),$$

$$x_5 = \frac{S_i}{\rho_* A}\left(\frac{\partial\tau_{iL}}{\partial\epsilon_L} - \frac{\partial\tau_i}{\partial\epsilon_L} + \frac{u_G}{\epsilon_G}\frac{\partial\tau_{iL}}{\partial u_G} - \frac{u_G}{\epsilon_G}\frac{\partial\tau_i}{\partial u_G} - \frac{u_L}{\epsilon_L}\frac{\partial\tau_{iL}}{\partial u_L} + \frac{u_L}{\epsilon_L}\frac{\partial\tau_i}{\partial u_L}\right),$$

and where the viscous stresses are modelled as

$$\tau_L = \frac{1}{2}f_L\rho_L u_L^2, \quad f_L = C_L\left(\frac{D_L u_L}{\nu_L}\right)^{-n_L}, \quad D_L = 4d_L,$$

$$\tau_G = \frac{1}{2}f_G\rho_G u_G^2, \quad f_G = C_G\left(\frac{D_G u_G}{\nu_G}\right)^{-n_G}, \quad D_G = 2d_G,$$

$$\tau_i = \frac{1}{2}f_i\rho_G(u_G - u_L)|u_G - u_L|,$$

$$\tau_{iL} = \frac{\tau_L\epsilon_G - \tau_G\epsilon_L}{\epsilon_L + \epsilon_G}.$$

The coefficients C_G and C_L both take the value 0.046 for turbulent flow and 16 for laminar flow, while n_L and n_G both take the value 0.2 for turbulent flow, and 1.0 for laminar flow. Finally, the interfacial friction factor f_i is assumed to be constant and equal to 0.0142 (see Barnea (1991)).

References

Abrams, J., Hanratty, T.J., 1985. Relaxation effects observed for turbulent flow over a wavy surface. J. Fluid Mech. 151, 443–455.

Acheson, D.J., 1990. Elementary Fluid Dynamics. Oxford University Press.

Adjoua, S., Magnaudet, J., 2009. Développement d'une méthode de simulation á un fluide découlements diphasiques turbulents. In: 19e mé Congrés Français de Mécanique.

Akai, M., Isoue, A., Aoki, S., Endo, K., 1980. A co-current stratified air-mercury flow with wavy interface. Int. J. Multiphase Flow 6, 173–190.

Akai, M., Isoue, A., Aoki, S., Endo, K., 1981. The prediction of stratified two-phase flow with a two-equation model of turbulence. Int. J. Multiphase Flow 7, 21–39.

Barnea, D., 1991. On the effect of viscosity on stability of stratified gas–liquid flow – application to flow pattern transition at various pipe inclinations. Chem. Eng. Sci. 46, 2123–2131.

Belcher, S.E., Hunt, J.C.R., 1993. Turbulent shear flow over slowly moving waves. J Fluid Mech. 251, 109–148.

Belcher, S.E., Hunt, J.C.R., 1998. Turbulent flow over hills and waves. Ann. Rev. Fluid Mech. 30, 507.

Belcher, S.E., Harris, J.A., Street, R.L., 1994. Linear dynamics of wind waves in coupled turbulent air–water flow. Part 1. Theory. J. Fluid Mech. 271, 119–151.

Benjamin, T.B., 1958. Shearing flow over a wavy boundary. J. Fluid Mech. 6, 161–205.

Biberg, D., 2007. A mathematical model for two-phase stratified turbulent duct flow. Multiphase Sci. Technnol. 19, 1–48.

Boeck, T., Li, J., Lopez-Pages, E., Yecko, P., Zaleski, S., 2007. Ligament formation in sheared liquid–gas layers. Theor. Comput. Fluid Dyn. 21, 59–76.
Boomkamp, P.A.M., Miesen, R.H.M., 1996. Classification of instabilities in parallel two-phase flow. Int. J. Multiphase Flow 22, 67–88.
Bradshaw, P., 1974. Possible origin of Prandtl's mixing-length theory. Nature 249, 135.
Chandrasekhar, S., 1961. Hydrodynamic and Hydromagnetic Stability. Dover, New York.
Cohen, L.S., Hanratty, T.J., 1965. Generation of waves in the concurrent flow of air and a liquid. AIChE Journal, 11–138.
Craik, A.D.D., 1966. Wind-generated waves in thin liquid films. J. Fluid Mech. 26, 369–392.
Fulgosi, M., Lakehal, D., Banerjee, S., De Angelis, V., 2002. Direct numerical simulations of turbulence in a sheared air–water flow with a deformable interface. J. Fluid Mech. 482, 319–345.
Fuster, D., Bague, A., Boeck, T., Le Moyne, L., Leboissetier, A., Popinet, S., Ray, P., Scardovelli, R., Zaleski, S., 2009. Simulation of primary atomization with an octree adaptive mesh refinement and VOF method. Int. J. Multiphase Flow 35, 550–565.
Hall-Taylor, N.S., Hewitt, G.F., 1970. Annular Two-Phase Flows. Pergamon Press, Oxford.
Hooper, A.P., Boyd, W.G.C., 1983. Shear-flow instability at the interface between two viscous fluids. J. Fluid Mech. 128, 507–528.
Ierley, G., Miles, J., 2001. On Townsend's rapid-distortion model of the turbulent-wind-wave problem. J. Fluid Mech. 435, 175–189.
Janssen, P.A.E.M., 2004. The Interaction of Ocean Waves and Wind. Cambridge University Press, Cambridge, UK.
Kelly, R.E., Goussis, D.A., 1989. The mechanism for surface wave instability in film flow down an inclined plane. Phys. Fluids A 1, 819–828.
Kuru, W.C., Sangalli, M., Uphold, D.D., McCready, M.J., 1995. Linear stability of stratified channel flow. Int. J. Multiphase Flow 21, 733–753.
Lin, M.-Y., Moeng, C.-H., Tsai, W.-T., Sullivan, P.P., Belcher, S.E., 2008. Direct numerical simulation of wind-wave. J. Fluid Mech. 616, 1–30.
Miesen, R., Boersma, B.J., 1995. Hydrodynamic stability of a sheared liquid film. J. Fluid Mech. 301, 175–202.
Miles, J.W., 1957. On the generation of surface waves by shear flows. J. Fluid Mech. 3, 185–204.
Monin, A.S., Yaglom, A.M., 1971. Statistical Fluid Mechanics: Mechanics of Turbulence. MIT Press, Cambridge, MA.
Morland, L.C., Saffman, P.G., 1993. Effect of wind profile on the instability of wind blowing over water. J. Fluid Mech. 252, 383–398.
M'F Orr, W., 1907a. The stability or instability of the steady motions of a perfect liquid and of a viscous liquid. Part I. Proc. Roy. Irish Acad. 27, 9–138.
M'F Orr, W., 1907b. The stability or instability of the steady motions of a perfect liquid and of a viscous liquid. Part II. Proc. Roy. Irish Acad. 27, 69–138.
Orszag, S.A., 1971. Accurate solution of the Orr–Sommerfeld stability equation. J. Fluid Mech. 50, 689–703.
Phillips, O.M., 1957. On the generation of waves by turbulent wind. J. Fluid Mech. 2, 417–445.
Pope, S.B., 2000. Turbulent Flows. Cambridge University Press, Cambridge, UK.
Shapiro, E., Timoshin, S., 2005. On the patterns of interaction between shear and interfacial modes in plane air–water poiseuille flow. Proc. Roy. Soc. A 461, 1583.
Solbakken, S., Andersson, H.I., 2004. On the drag reduction mechanism in a lubricated turbulent channel flow. Int. J. Heat Fluid Flow 25, 618.
Spalart, P.R., 1988. Direct simulation of a turbulent boundary layer up to $r_\theta = 1410$. J. Fluid Mech. 187, 61–98.
Sullivan, P.P., McWilliams, J., Moeng, C.-H., 2000. Simulation of turbulent flow over idealized water waves. J. Fluid Mech. 404, 47–85.
Ó Náraigh, L., Spelt, P.D.M., 2010. Interfacial instability of turbulent two-phase stratified flow: pressure-driven flow and non-newtonian layers. J. Non-Newt. Fluid Mech. 165, 489–508.
Townsend, A.A., 1972. Flow in a deep turbulent boundary layer over a surface distorted by water waves. J. Fluid Mech. 55, 719–735.
Townsend, A.A., 1980. The response of sheared turbulence to additional distortion. J. Fluid Mech. 81, 171–191.
Valluri, P., Spelt, P.D.M., Lawrence, C.J., Hewitt, G.F., 2008. Numerical simulation of the onset of slug initiation in laminar horizontal channel flow. Int. J. Multiphase Flow 34, 206–225.
Valluri, P., Ó Náraigh, L., Ding, H., Spelt, P.D.M., 2010. Linear and nonlinear spatio-temporal instability in laminar two-layer flows. J. Fluid Mech. 656, 458–480.
Willmarth, W.W., Wei, T., Lee, C.O., 1987. Laser anemometer measurements of reynolds stress in a turbulent channel flow with drag reducing polymer additives. Phys. Fluids 30, 933.
Yecko, P., Zaleski, S., Fullana, J.-M., 2002. Viscous modes in two-phase mixing layers. Phys. Fluids 14, 4115.
Yiantsios, S.G., Higgins, B.G., 1988. Linear stability of plane Poiseuile flow of two superposed fluids. Phys. Fluids 31, 3225–3238.
Yih, C.S., 1967. Instability due to viscosity stratification. J. Fluid Mech. 27, 337–352.
Zilker, D.P., Cook, G.W., Hanratty, T.J., 1976. Influence of the amplitude of a solid wavy wall on a turbulent flow. Part 1. Non-separated flows. J. Fluid Mech. 82, 29–51.